

Article

Impregnation of Modified Magnetic Nanoparticles on Low-Cost Agro-Waste-Derived Biochar for Enhanced Removal of Pharmaceutically Active Compounds: Performance Evaluation and Optimization Using Response Surface Methodology

Arif Jamal Siddiqui ^{1,*}, Nisha Kumari ^{2,†}, Mohd Adnan ¹, Sanjeev Kumar ³, Abdelmushin Abdelgadir ¹, Juhi Saxena ⁴, Riadh Badraoui ^{1,5}, Mejdi Snoussi ^{1,6}, Puja Khare ⁷ and Ritu Singh ^{2,*}

¹ Department of Biology, College of Science, University of Ha'il, Ha'il P.O. Box 2440, Saudi Arabia; drmohdadnan@gmail.com (M.A.); abdelmuhsin@yahoo.com (A.A.); badraouir@yahoo.fr or riadh.badraoui@fmt.utm.tn (R.B.); snmejdi@yahoo.fr (M.S.)

² Department of Environmental Science, School of Earth Sciences, Central University of Rajasthan, Ajmer 305817, India; nishasinghevs123@gmail.com

³ School of Earth and Environmental Sciences, Babasaheb Bhimrao Ambedkar University, Lucknow 226025, India; sanjivk845@gmail.com

⁴ Department of Biotechnology, University Institute of Biotechnology, Chandigarh University, Ludhiana 140413, India; juhi.e12213@cumail.in

⁵ Section of Histology-Cytology, Medicine Faculty of Tunis, University of Tunis El Manar, Tunis 1017, Tunisia

⁶ Laboratory of Genetics, Biodiversity and Valorization of Bio-Resources (LR11ES41), Higher Institute of Biotechnology of Monastir, University of Monastir, Avenue Tahar Haddad, BP74, Monastir 5000, Tunisia

⁷ Plant Production and Protection Division, CSIR—Central Institute of Medicinal and Aromatic Plants, Lucknow 226015, India; pujakhare@cimap.res.in

* Correspondence: ar.siddiqui@uoh.edu.sa or arifjamal13@gmail.com (A.J.S.);

ritu_ens@curaj.ac.in or ritu2735@gmail.com (R.S.); Tel.: +966-557399031 (A.J.S.); +919-602127352 (R.S.)

† These authors contributed equally to this work.



Citation: Siddiqui, A.J.; Kumari, N.; Adnan, M.; Kumar, S.; Abdelgadir, A.; Saxena, J.; Badraoui, R.; Snoussi, M.; Khare, P.; Singh, R. Impregnation of Modified Magnetic Nanoparticles on Low-Cost Agro-Waste-Derived Biochar for Enhanced Removal of Pharmaceutically Active Compounds: Performance Evaluation and Optimization Using Response Surface Methodology. *Water* **2023**, *15*, 1688. <https://doi.org/10.3390/w15091688>

Academic Editors: Shahid Iqbal and Ali Bahadur

Received: 27 March 2023

Revised: 19 April 2023

Accepted: 21 April 2023

Published: 26 April 2023



Copyright: © 2023 by the authors. Licensee MDPI, Basel, Switzerland. This article is an open access article distributed under the terms and conditions of the Creative Commons Attribution (CC BY) license (<https://creativecommons.org/licenses/by/4.0/>).

Abstract: In the present study, a magnetic nanocomposite based on biochar (BC) derived from sugarcane bagasse, nanoscale zerovalent iron (nZVI), and chitosan (CS) was fabricated to investigate its efficacy for the removal of two widely used pharmaceutically active compounds (PhACs), namely aspirin (ASA) and carbamazepine (CBZ). The synthesized nanocomposite (BC-CS@nZVI) was characterized using XRD, FTIR, and FESEM-EDX. The Response Surface Methodology–Central Composite Design (RSM-CCD) model was used for the optimization of removal efficacies for both drugs using five variables, i.e., adsorbent dose (0.05–0.1 g), pH (2–10), drug concentration (20–40 ppm), time (40–80 min), and temperature (40–60 °C). Under optimized conditions of adsorbent dose: 0.075 g, pH: 2, drug concentration: 30 ppm, time: 60 min, and temperature: 50 °C, the maximum removal efficiency of ASA drug was observed to be 97.8%, while in the case of CBZ drug under similar conditions with pH 6, the maximum removal was found up to 89.32%. The isotherm models revealed that both ASA and CBZ adsorption data fit well with the Langmuir isotherm showing monolayer adsorption. The kinetics of adsorption was well explained by the pseudo-first- and pseudo-second-order models in the case of ASA and CBZ, respectively. Thermodynamic parameters confirmed the feasibility of the reaction and its spontaneous and exothermic nature. The reusability and efficiency in water samples of the Ha'il region were investigated to demonstrate its potential for practical application.

Keywords: aspirin; carbamazepine; sugarcane bagasse; Ha'il; biochar; chitosan; nZVI

1. Introduction

In recent years, the contamination of water resources by pharmaceutically active compounds (PhACs) has become a major issue of concern all over the world due to their increased demand in the health sector [1]. To address these demands, the rate of production

of various categories of PhACs, such as non-steroidal anti-inflammatory drugs (NSAIDs), antiseptics, antimicrobials, antiepileptics, antibiotics, tranquilizers, etc., has experienced a rapid surge in the past few decades [2]. Aspirin and carbamazepine are two such PhACs which are widely used in the society. Aspirin, also recognized as acetylsalicylic acid (ASA), is a common NSAID, having antipyretic and analgesic properties used to treat inflammation, cold-related headaches, renal functions, and other conditions, such as Alzheimer's disease, cancer, and cardiovascular diseases [3–5]. Another drug is carbamazepine (CBZ) which belongs to the class of benzodiazepines and is principally used to treat epileptic disorders [6]. CBZ is also used to treat bipolar illness, nerve diseases, psychiatric therapy, and trigeminal neuralgia, in addition to helping epileptic patients control their seizures [7]. The primary sources of the presence of these drugs in the environment include effluents generated from pharmaceutical manufacturing plants, hospitals, and households, runoff from agricultural farms, livestock, aquaculture industries, municipal wastewater treatment plants, and unregulated dumping of expired or unused drugs [8,9]. Several studies reported significant quantities of ASA and CBZ in surface water bodies, domestic effluents, and WWTPs, with concentrations ranging from 5 µg/L to 2 mg/L [10,11]. Both of these drugs have been reported to have adverse impacts on exposed organisms, even at very low concentrations. For instance, ASA exposure leads to gastrointestinal ulcers, tinnitus, DNA damage, induces oxidative stress, and has an inhibitory effect on blood platelets [12,13]. Similarly, CBZ exposure results in endocrine disruption, hepatic injuries, acute pneumonia, and lethal cardiovascular diseases and bears neurotoxicity and developmental toxicity [14,15]. Due to the persistency, recalcitrancy, and toxicity of ASA and CBZ, their removal from contaminated matrices is much needed.

In recent years, green, or environmentally friendly, adsorbents have gained ample attention in the area of pollution abatement due to their easy availability, low cost, environmental friendliness, and decent adsorption efficacies [16,17]. Green adsorbents are prepared mainly from agro-wastes, natural resources, aquatic biomass, etc., and have demonstrated significant removal efficiencies for varied contaminants [18,19]. However, biomass-based adsorbents have certain limitations, such as poor adsorptivity, low regeneration capacity, low stability, high sensitivity to pH and temperature changes, etc., which lowers their overall performance [20]. The conversion of biomass to high-value-added products, such as biochar, could address these shortcomings.

Biochar (BC) derived from agricultural by-products and residues has gained significant attention across the globe, as it promotes waste management practices, circular economy, environmental protection, and sustainability [21,22]. Earlier studies have reported that biochar has better treatment efficiency in comparison with its biomass counterparts due to its greater surface area, abundance of surface functional groups, high porosity, stability, etc. [23,24]. In recent times, attempts have been made to further enhance the efficiency of biochar by incorporating/modifying it with nanomaterials. For instance, biochar-incorporated Zn-Co-layered double hydroxide nanostructures were synthesized for the degradation of gemifloxacin, and the results revealed removal up to 92.7% [25]. In another study, olive stone biochar-supported Co₃O₄ nanoparticles were employed successfully for rifampicin and tigecycline removal from wastewater with 95.18% and 75.48% efficiency, respectively [26]. Similarly, biochar derived from banana pseudo-stem fibers impregnated with CoFe₂O₄ nanoparticles and a nitrogen-enriched Co@N-BC composite was successfully synthesized for the efficient removal of amoxicillin antibiotic and doxycycline, respectively [27,28]. The studies have reported significant removal of pharmaceutical drugs using nanomaterial-modified biochar, however, their separation from the aqueous solution is still a challenge, which could be addressed using magnetic-nanoparticle-incorporated biochar.

In the present study, we reported impregnation of biochar obtained from sugarcane bagasse with chitosan-modified magnetic zero-valent iron nanocomposite (BC-CS@nZVI) to simultaneously remove two PhACs, namely ASA and CBZ. Table 1 displays the physico-chemical properties of both the drugs. Sugarcane-bagasse-based biochar has been selected in this study, as India shares 20% of the global production of sugarcane, with each ton of

sugarcane processing yielding ~260 kg of sugarcane bagasse [21]. Chitosan has been used herein for surface modification of nZVI, which prevents surface oxidation and aggregation of nZVI, thereby increasing its reactivity and practical applicability [29,30]. The primary objective of this research includes (a) investigation of the effectiveness of synthesized BC-CS@nZVI for removing ASA and CBZ drugs from aqueous solution; (b) optimization of the process parameters influencing drug adsorption using Response Surface Methodology–Central Composite Design (RSM-CCD), and (c) elucidation of reaction mechanism via adsorption isotherms and kinetic models. Further reusability of BC-CS@nZVI and its application in real water samples collected from the Ha'il region was investigated.

Table 1. Physico-chemical properties of ASA and CBZ.

S.No.	Property	ASA	CBZ
1.	Molar mass	180.16 g/mol	236.27 g/mol
2.	pKa	3.49	15.96
3.	Solubility	<1 mg/mL	>35.4 ug/mL
4.	Density	1.4 ± 0.1 g/cm ³	1.3 ± 0.1 g/cm ³
5.	Boiling point	140 °C	411.0 ± 48.0 °C

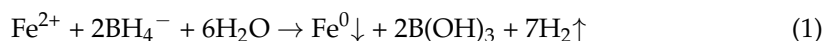
2. Materials and Methods

2.1. Materials

CBZ (% assay: 99.00%) and ASA (% assay: 98.00%) drug was acquired from Himedia laboratories private limited, Mumbai, Maharashtra, India. Iron (II) sulphate heptahydrate (FeSO₄·7H₂O), chitosan from shrimp shells (C₅₆H₁₀₃N₉O₃₉), and sodium borohydride (NaBH₄) were purchased from Sigma Aldrich, St. Louis, MI, USA.

2.2. Synthesis of BC-CS@nZVI

The preparation method and characteristics of the biochar derived from sugarcane bagasse are reported in a previous study [24]. Herein, the wet chemical reduction method was employed for the synthesis of biochar-incorporated chitosan-modified nZVI (BC-CS@nZVI) with minor changes in the method reported by [31,32]. In brief, 0.75 g of the biochar was dissolved in 0.027 M solution of FeSO₄·7H₂O in 100 mL of deionized water and mixed for one hour with a magnetic stirrer. After that, 0.5% *w/v* of chitosan containing 1% acetic acid was added and ultra-sonicated for 2 h. To the solution freshly prepared solution, 0.108 M NaBH₄ was added dropwise and then continuously stirred for one hour. When the prepared borohydride solution was added to the precursor mixture, a black-coloured precipitate was instantly formed, indicating the complete reduction of ferrous iron (Fe²⁺ to zero-valent iron (Fe⁰)). The underlying mechanism could be attributed to the occurrence of redox reaction represented in the following equation:



The precipitate was collected by filtration and then washed several times with ethanol and distilled water. Lastly, the formed nanocomposite was allowed to dry and then stored in a closed vessel in an inert condition.

2.3. Point of Zero Charge (pH_{pzc})

It is important to determine the point of zero charge (pH_{pzc}) of the BC-CS@nZVI in order to identify the best pH at which the adsorbent will function most effectively. In the present study, the salt addition technique was used to calculate the (pH_{pzc}) value of the adsorbent [33]. In accordance with the procedure, a solution of sodium nitrate (0.05 M) was prepared in 40 mL of distilled water. The solution was prepared in a series in 50 mL of beaker with initial pH (pH_i) adjusted between 2 and 9 with hydrochloric acid (0.1 M)

and sodium hydroxide (0.1 M), and 1 g of adsorbent was added into each beaker and kept on a shaker for 48 h at room temperature. After the shaking was completed, the sample was centrifuged to separate the adsorbent from the solution, and the final pH was measured using the same method mentioned above. The graph was plotted between $\Delta\text{pH} = (\text{pH}_f - \text{pH}_i)$ vs. pH_i to evaluate the pH_{pzc} value of BC-CS@nZVI.

2.4. Instrumentation

The phase identification, size, surface morphologies, elemental composition, and functional groups of the synthesized nanocomposite were determined using an X-ray diffractometer (XRD) (PANalytical Empyrean), field-emission scanning electron microscope (FE-SEM) coupled with energy dispersive X-ray (EDX) (Merlin Compact, Carl Zeiss), and Fourier transform infrared (FT-IR) spectroscopy (PerkinElmer), respectively.

2.5. Batch Experiments

To evaluate the efficacy of the prepared nanocomposite for ASA and CBZ removal, the experiments were conducted using the desired amount of BC-CS@nZVI mixed in 40 mL of ASA and CBZ solution (100 ppm). The initial removal experiment was conducted at the natural pH of the ASA and CBZ solution, i.e., 4.25 and 6.72, respectively. The pH of the drug solution was measured using Labtronics microprocessor digital pH meter. For optimization, ranges of the influencing parameters were set to investigate the maximum removal efficiency of BC-CS@nZVI for ASA and CBZ drug. The pH of the drugs solution was varied from 2 to 10 using NaOH and HCl of 0.1 M solutions, the dose of adsorbent varied from 0.05 to 0.1 g, ASA/CBZ concentration was altered from 20 to 40 ppm, temperature variation ranged from 40 to 60 °C, and the contact time was varied in the range from 40 to 80 min. The reaction mixture was then kept on a shaker for a predetermined time interval and then centrifuged. The remaining concentration of ASA and CBZ in the supernatant solution was measured at 236 nm and 284 nm, respectively, on a Cary 100 UV-Vis spectrophotometer. All the experiments were conducted in triplicate. The ASA/CBZ removal percent ($R\%$) and adsorption capacities at equilibrium (q_e) (mg/g) were determined using Equations (2) and (3):

$$R\% = \frac{C_o - C_e}{C_o} \times 100 \quad (2)$$

$$q_e = \frac{C_o - C_e}{W} \times V \quad (3)$$

where, C_o (ppm) is the initial ASA/CBZ concentration, C_e is the amount of ASA/CBZ residue in the sample, W denotes the BC-CS@nZVI dose (g), and V is the volume of the solution (L). Reaction kinetics, adsorption isotherms, and thermodynamic parameters were studied using suitable models and are described in Section 3.

2.6. Optimization of Process Parameters through RSM-CCD

RSM-CCD is a valuable tool for designing, enhancing, and optimizing process parameters in a multivariable system [34]. In contrast to the traditional OVAT (one-variable-at-a-time) approach, the RSM-CCD model reduces the number of experimental runs required for investigating the simultaneous interaction of process variables and their effect on response, saving a lot of time and cost. Herein, the optimization of ASA and CBZ removal was carried out by RSM-CCD using five independent variables, viz. concentration of drugs, pH, time, BC-CS@nZVI dose, and temperature. The low level and high level were coded as -1 and $+1$, respectively, for the independent variables (Table 2).

Table 2. Experimental range and levels of independent process variables.

Independent Variable	Units	Symbol	Coded Levels			
			−alpha	−1	+1	+alpha
Drug concentration	ppm	A	10.00	20.00	40.00	50.00
Contact time	min	B	20.00	40.00	80.00	100.00
pH	...	C	2.00	4.00	8.00	10.00
Adsorbent dose	g	D	0.025	0.05	0.1	0.125
Temperature	°C	E	30.00	40.00	60.00	70.00

The number of experiments (N) needed in a 2⁵ factorial CCD for five independent variables was calculated using Equation (4) [35]:

$$N = 2^n + 2n + n_c \quad (4)$$

where n = 5, number of independent variables; and n_c = 6, central point's number. Thus, 32 experiments were performed to create a model equation and identify the optimized condition to obtain the maximum response (Table 3).

Table 3. Central composite design matrix and its actual and predicted values for both ASA and CBZ.

S. NO.	Drug Concentration (ppm)	Time (min)	pH	Adsorbent Dose (g)	Temperature (°C)	% REMOVAL			
						ASA		CBZ	
						Expt.	Pred.	Expt.	Pred.
1	40	80	8	0.1	60	54	55.32	64.27	65.35
2	40	40	4	0.1	60	85.32	85.67	50.2	51.40
3	20	80	8	0.1	40	65	65.97	70.28	71.66
4	40	40	4	0.05	40	75.98	76.01	40.36	41.38
5	20	80	4	0.1	60	96.2	96.06	47.33	48.43
6	20	80	4	0.05	40	91.3	90.84	42.53	43.45
7	30	60	6	0.075	30	77.61	76.61	76.39	73.76
8	20	40	8	0.05	40	41.6	42.39	70.96	72.08
9	30	60	6	0.075	50	76.21	69.53	88.56	88.19
10	40	40	8	0.1	40	49	50.46	66.05	67.53
11	30	60	6	0.075	70	77.812	76.80	82.21	80.52
12	30	60	6	0.125	50	78	76.35	76.23	73.24
13	20	40	8	0.1	60	55.21	56.33	76.29	77.60
14	30	60	6	0.075	50	65	69.53	88.39	88.19
15	30	60	6	0.025	50	58.32	57.96	77.96	76.64
16	30	20	6	0.075	50	60.56	59.26	78.65	76.16
17	30	60	6	0.075	50	65.2	69.53	89.32	88.19
18	40	40	8	0.05	60	38	39.14	78.69	79.51
19	30	60	6	0.075	50	70.8	69.53	88.21	88.19
20	30	60	10	0.075	50	33.84	30.61	69.2	66.95
21	10	60	6	0.075	50	75.25	74.94	75.2	72.91
22	20	80	8	0.05	60	52	52.65	83.21	83.94
23	50	60	6	0.075	50	62.8	61.10	71.32	69.29
24	40	80	4	0.1	40	85	85.21	62.98	64.25
25	30	60	2	0.075	50	97.89	99.11	28.64	26.57
26	40	80	4	0.05	60	79.89	79.77	59.62	60.24
27	30	100	6	0.075	50	73.25	72.54	78.2	76.37
28	20	40	4	0.05	60	82	81.68	62.25	63.10
29	20	40	4	0.1	40	88	88.01	61.54	63.04
30	40	80	8	0.05	40	46	46.99	78.25	79.15
31	30	60	6	0.075	50	67.98	69.53	85.32	88.19
32	30	60	6	0.075	50	69.98	69.53	85.02	88.19

Notes: Expt. = Experimental value; Pred. = Predicted value.

The prediction of the response, i.e., removal efficiency of BC-CS@nZVI for ASA and CBZ, was carried out using the mean of triplicate experimental observations that was fed into the experimental matrix to obtain a regression model equation [36]. To determine the optimal removal conditions for ASA and CBZ, the data were eventually modelled to correlate the relationship between removal efficiency and the independent variables using a quadratic polynomial equation (Equation (5) [32]).

$$Y = \beta_0 \sum_{i=1}^n \beta_i x_i + \beta_0 \sum_{i=1}^n \beta_{ii} x_i^2 + \sum_{i=1}^{n-1} \sum_{j=i+1}^n \beta_{ij} x_i x_j \quad (5)$$

where Y is the response; x_i and x_j are independent variables (i and j varying from 1 to n); β_0 is the constant term; β_i is the linear coefficient, β_{ij} is the interaction coefficient, β_{ii} is the quadratic coefficient; and n is the number of independent variables. The polynomial equation is based primarily on the estimation of the ordinary least squares, which helps to minimize the SSE (sum of squared errors) when evaluating the predicted values of the response (dependent variable). Further, to assess the model's adequacy and to calculate the coefficients of the individual and interacting model parameters, analysis of variance (ANOVA) was applied. Based on the p -value and F -value, significant model terms were chosen [37]. The correlation coefficient (R^2) was utilized to assess how well the quadratic model fitted the experimentally measured efficiency of drug removal. Regression analysis, evaluation of the statistical significance of model equations, and response optimization were all performed using Design Expert (Trial version 12).

2.7. Reusability

The adsorption–desorption study was conducted to investigate the reusability of BC-CS@nZVI using ethanol as the desorption solvent. The experiments were carried out under optimized conditions of adsorbent dose: 0.075 g, drug concentration: 30 ppm, time: 60 min, temperature: 50 °C, pH 2 in the case of ASA, and pH 6 in the case of CBZ, for 5 consecutive cycles to evaluate the practical and economic value of the process. After the adsorption process, BC-CS@nZVI, was soaked in 40 mL of the ethanol solution and stirred for 180 min followed by centrifugation for 5 min at 4000 rpm. The adsorbent was washed 5 times with ethanol and distilled water to remove the excess ethanol and then dried for 3 h for further reuse.

2.8. Application in Real Water Samples

The removal efficiency of the synthesized nanocomposite for ASA and CBZ was examined under optimized conditions in real water samples collected from the Ha'il region. Two samples were collected from sewage and three from tap water. From each sample, 30 mL was taken and filtered, then it was spiked with the known concentration of both ASA and CBZ (30 ppm). Then, 0.075 g of nanocomposite was added to the spiked samples and studied under optimized pH, temperature, and contact time. After 60 min, all the samples were centrifuged and analyzed to obtain the removal percentage of both the drugs.

3. Results and Discussion

3.1. Characterization of the Synthesized BC-CS@nZVI Magnetic Nanocomposite

3.1.1. XRD

The phase structure of chitosan (CS), biochar (BC), nZVI, and BC-CS@nZVI was studied using X-ray diffraction (XRD) within the 2θ range of 50 to 70°. Figure 1(a) shows two broad diffraction peaks at 9.50° and 20.08°, corresponding to the reflection plane of 020 and 120, respectively, which are the typical fingerprints of chitosan with semi-crystalline structure [38,39]. The low intensity peaks observed at $2\theta = 16.53^\circ, 20.8^\circ, 40.5^\circ,$ and 50.08° are indicative of cellulose and hemicellulose constituents of biochar, as seen in Figure 1(b) [40], while the diffraction peak present at 26.5° corresponds to SiO_2 , which is the only crystalline phase in the biochar structure [41]. Bare nZVI displayed a sharp crystalline

characteristic peak at 44.9° , corresponding to the plane 110 (Figure 1(c)) [42], which was also evident in the XRD pattern of the BC-CS@nZVI, indicating successful loading of nZVI particles on the composite (Figure 1(d)). The crystallinity of the nanoparticles remained intact, likely due to the presence of CS in the nanocomposite. The broad and low-intensity peaks observed between 8.45° and 27.2° could be attributed to the presence of biochar in the composite [43]. The absence of iron oxide phases in BC-CS@nZVI indicates that CS and BC impede the oxidation of nZVI, enhancing the longevity and practical application of the composite. The size of the synthesized nanocomposite was determined using the Scherrer equation and was found to be 20.05 nm.

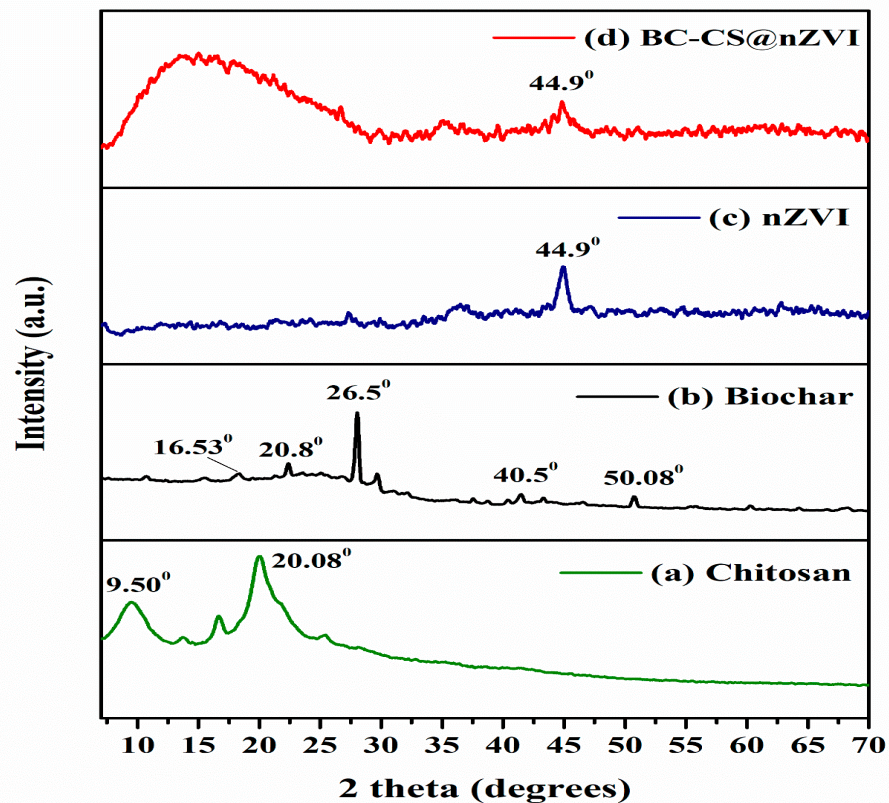
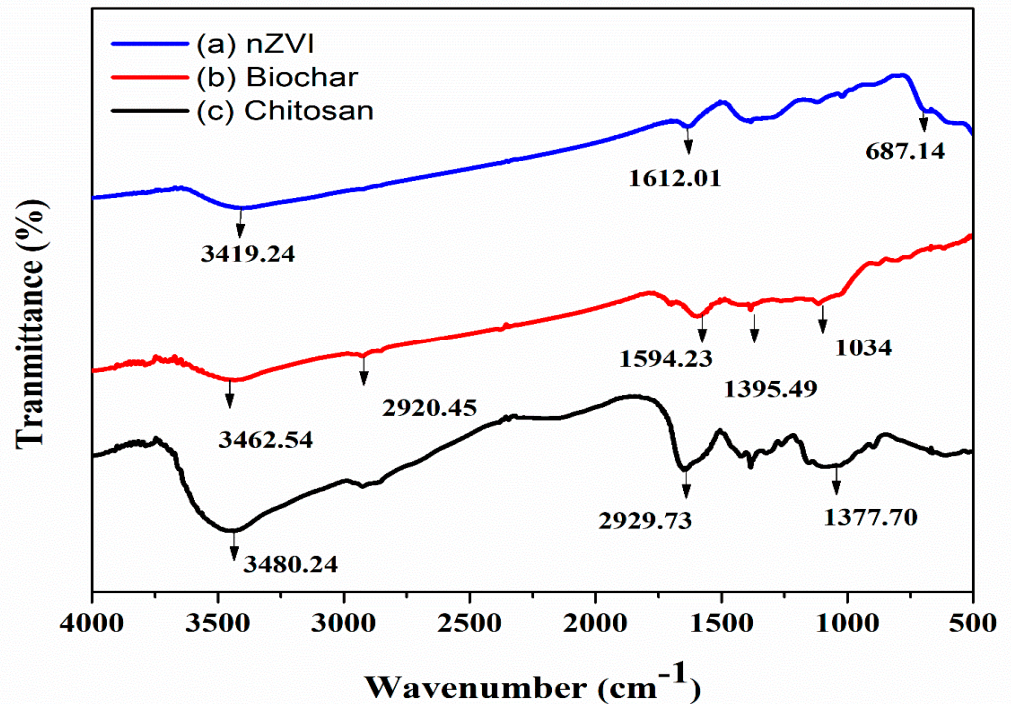


Figure 1. XRD image of (a) Chitosan, (b) Biochar, (c) bare nZVI, and (d) BC-CS@nZVI.

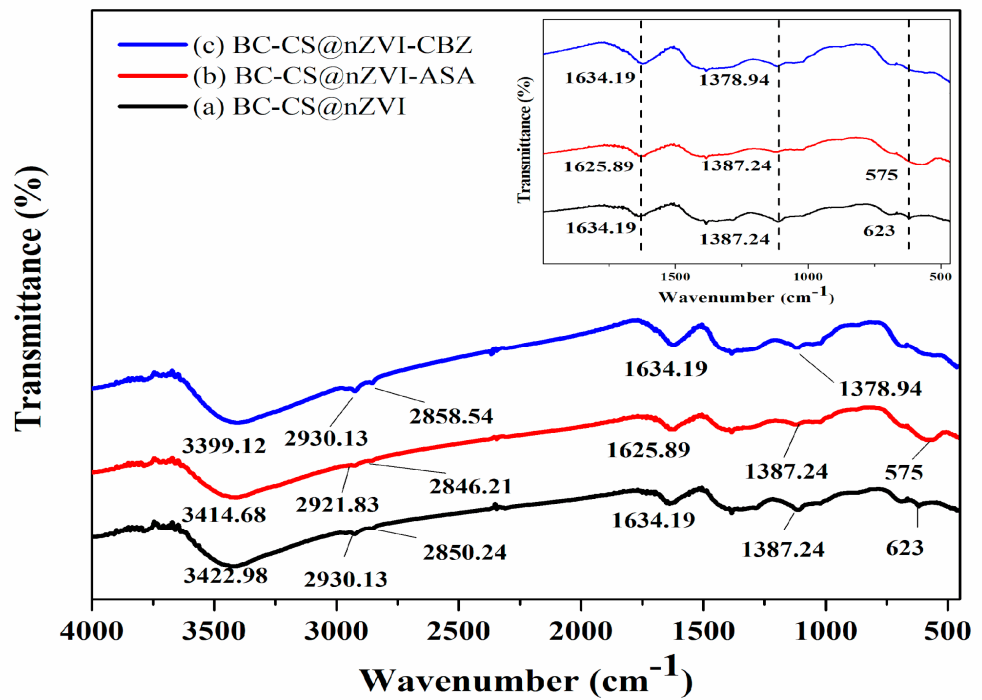
3.1.2. FTIR

The molecular fingerprints of the functional groups present on the surface of the adsorbent are displayed in Figure 2. The FTIR spectra of nZVI were acquired in the range of $500\text{--}4000\text{ cm}^{-1}$, as shown in Figure 2A(a). Here, the peaks of absorption observed at 687.14 cm^{-1} correspond to Fe-O stretching vibration. The absorption peak appeared at 3419.24 cm^{-1} and 1612.07 cm^{-1} , corresponding to the O-H stretching and bending vibration of water molecules adsorbed onto the nZVI surface. This suggests the formation of a ferric oxyhydroxide (FeOOH) layer on nZVI [44]. Similarly, the peak observed at 3462.54 cm^{-1} represents the stretching vibration of hydroxyl functional groups of water molecules present on the surface of biochar, as shown in Figure 2A(b). The peak at 2920.4 cm^{-1} is assigned to aliphatic group CH_2 present in the biochar structure. The peak at 1594.23 cm^{-1} corresponds to the C=O vibrations in hemicellulose. Further, the peak at 1395.49 cm^{-1} may be attributed to the C-O stretching in cellulose and hemicellulose, respectively. The peak observed at 1034 cm^{-1} is due to stretching vibration of the C-OH bond, corresponding to the polysaccharides and lignin present in biochar [45,46]. As shown in Figure 2A(c), the characteristic peak at 2929.73 cm^{-1} is attributed to the stretching vibration of C-H bond of the alkyl groups present in chitosan. The characteristic peak at 1377.70 cm^{-1} and

3480.24 cm^{-1} may be ascribed to the O–H and N–H stretching vibrations, indicating the amide (II) and hydroxyl groups of chitosan, respectively [32,47].



(A)



(B)

Figure 2. (A) FTIR spectra of (a) nZVI, (b) biochar, and (c) chitosan; (B) FTIR spectra of (a) BC-CS@nZVI before adsorption, (b) BC-CS@nZVI after ASA adsorption, and (c) BC-CS@nZVI after CBZ adsorption.

The FTIR spectra of various functional groups present on the surface of BC-CS@nZVI before and after adsorption of aspirin (ASA) and carbamazepine (CBZ) are shown in Figure 2B. The functional groups of individual components of BC-CS@nZVI nanocomposites can be seen on the surface of BC-CS@nZVI with slight or no prominent shifts (Figure 2B(a)). The characteristic peak at approximately 3422.98 cm^{-1} may be attributed to the stretching vibrations of the N-H and O-H groups, corresponding to the amide (II) and hydroxyl groups present in the structure of chitosan, respectively [48]. The stretching vibration of the -CH and -CH₂ bond of the alkyl groups and C=C (aromatic) groups of chitosan and biochar are represented at 2930.13 cm^{-1} and 2850.24 cm^{-1} , respectively [48,49]. The peak at 1634.19 cm^{-1} is attributed to the stretching vibration of C=O of -NH-C=O present in CS or carbonyl present in carboxyl group of the biochar [50]. The peak at approximately 1387.24 cm^{-1} is ascribed to the stretching vibration of N-O, which further indicates successful loading of chitosan on the BC-CS@nZVI structure [51]. The asymmetrical vibration of FeO was present at 623 cm^{-1} , signifying the existence of iron in BC-CS@nZVI structure [42,52,53]. The above finding indicates that biochar was successfully impregnated with CS@nZVI. The FTIR spectra of BC-CS@nZVI after adsorption of ASA and CBZ are shown Figure 2B(b,c). After adsorption, the peaks at approximately 3422.98 (-OH and -NH bond) in BC-CS@nZVI were shifted to 3414.68 cm^{-1} and 3399.12 cm^{-1} , while the peak at 1387.24 cm^{-1} (N-O) shifted to 1378.94 cm^{-1} in CBZ-adsorbed BC-CS@nZVI. The 1634.19 cm^{-1} (C=O) peak was shifted to 1625.89 cm^{-1} after adsorption of the ASA drug, while its intensity increased slightly in the case of CBZ. In addition, the 623 cm^{-1} peak (Fe=O) shifted to 575 cm^{-1} in ASA, but it disappeared in the CBZ spectra, which could be due to the participation of Fe=O bond in the removal of carbamazepine drug. The reason behind shifting of the peaks observed after removal of the drugs and changes in their intensity may be due to the substitution of active sites present on BC-CS@nZVI by drug molecules, which results in the alteration in the surface composition of the composite.

3.1.3. FE-SEM/EDX

The surface morphologies of the nanocomposite before and after adsorption of ASA and CBZ are shown in Figure 3. Biochar is known to have a porous structure that provides a favorable platform for loading of the nanomaterials [54,55]. In the present study, chain-like nanostructures of CS@nZVI arranged in a branched and zigzagged manner have been seen over the surface of BC-CS@nZVI (Figure 3a). The linear orientation of the nanoparticles could be due to the magnetic dipole-dipole interaction of iron [42,56], and the prevention of aggregation of the nanoparticles could be ascribed to the electrostatic repulsion and steric hindrance provided by chitosan and biochar. The role of chitosan and biochar in stabilization of the nanoparticles and prevention of their oxidation is well documented [57–59] and has been reported in our previous study [32]. The porous structure of the biochar is not apparent in the image possibly due to the blockage of the pore channels with the modified nanoparticles [50]. The microsphere structure present over the BC surface enhances the surface area of the BC-CS@nZVI, thereby increasing its removal capacity by providing more active sites for adsorption and other reactions [60]. Figure 3b,c display the surface of the nanocomposite after adsorption of ASA and CBZ, respectively. The images show deposition of the target compounds on the surface removing the crisp and defined structures of BC-CS@nZVI. The surface of the nanocomposite was observed to be rougher and more irregular, with the appearance of some flocculent particles that illustrate uneven and bulk attachment of ASA and CBZ molecules on the surface nanocomposite, endorsing its spontaneity and effectiveness for drug removal [32,61]. EDX analysis showed the elemental composition of BC-CS@nZVI before and after adsorption of ASA and CBZ. As illustrated in Figure 3a, the presence of Fe (31.92%) confirms the existence of iron nanoparticles in the synthesized nanocomposite. The presence of C (21.86%), N (12.21%), and some amount of mineral fractions, such as Si (0.8%), K (2.59%), Ca (0.19%), and K (2.59%), confirms successful loading of CS@nZVI on the biochar. The existence of O (28.46%) could be attributed to partial oxidation of nZVI. After adsorption of the drugs,

an increase in the carbon and oxygen percentages from 56.26% and 26.08% in the case of ASA and 51.01% and 30.04% in the case of CBZ was noticed (Figure 3b,c). On the contrary, a decline in the Fe percentage to 0.05% and 1.22% was observed in ASA and CBZ, respectively. The increase observed in the carbon and oxygen percentages could be ascribed to the accumulation of ASA and CBZ molecules or its intermediates on the surface of the nanocomposite, while the decrease in Fe percentage could be due either to accumulation of target molecule/intermediates or to dissolution of iron at lower pH conditions [62].

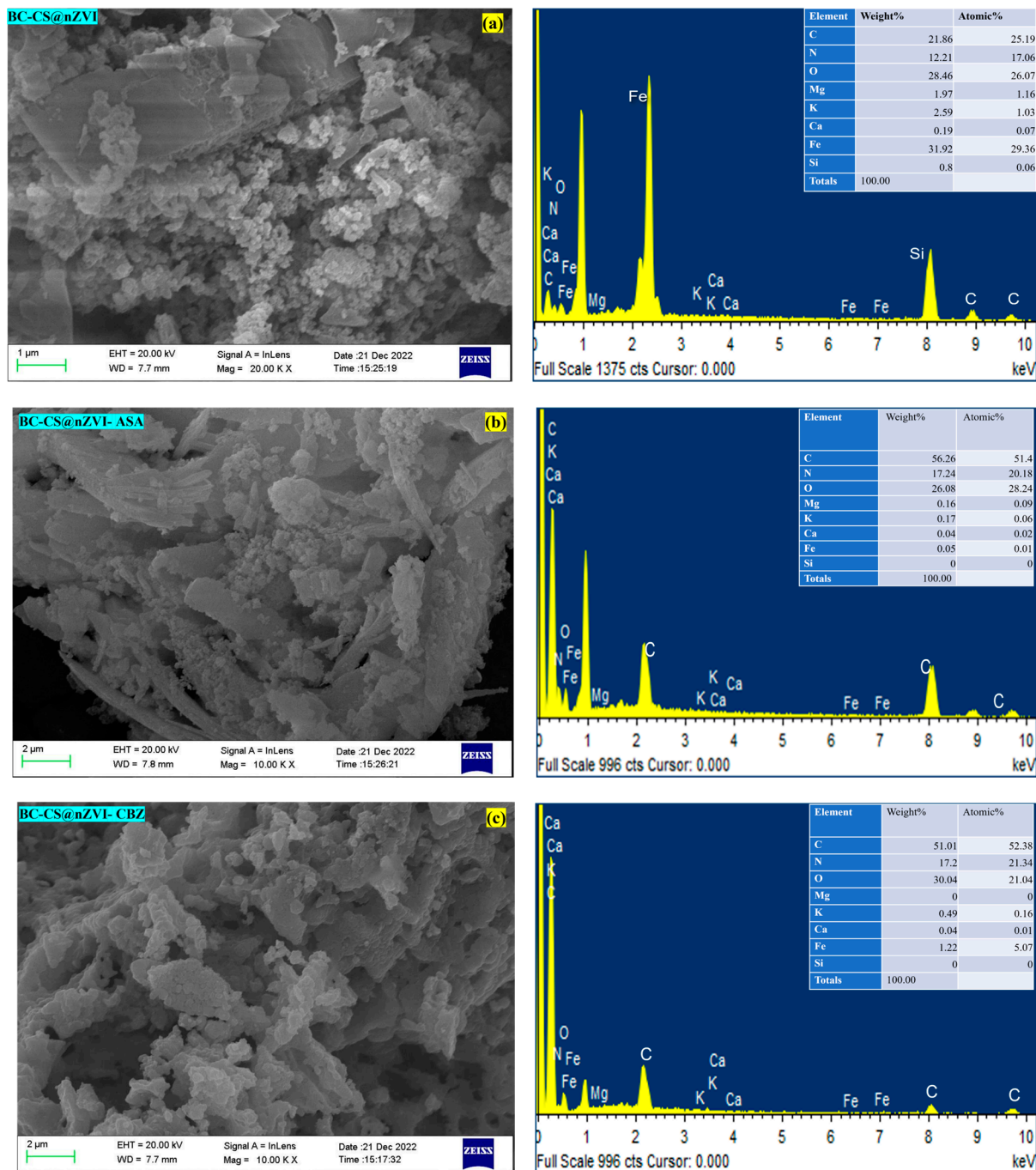


Figure 3. SEM and EDX pattern of (a) BC-CS@nZVI before adsorption, (b) BC-CS@nZVI after adsorption of ASA, and (c) BC-CS@nZVI after adsorption of CBZ.

3.2. Optimization of Process Variables Using RSM-CCD

RSM-CCD was used herein to optimize five variable factors for the removal of ASA and CBZ using BC-CS@nZVI magnetic nanocomposite. The experimental results of the removal (%) of ASA and CBZ using five factors CCD experimental design are displayed in Table 3.

3.2.1. Model Fitting and ANOVA Analysis

The ANOVA results shown in Tables 4 and 5 provide the calculated response of the quadratic surface model. It determines the acceptability of the response generated by the quadratic model for representing ASA and CBZ drug removal by BC-CS@nZVI. The result in the present study indicates that the coefficient of the linear effect in the case of ASA for all the factors ($p < 0.05$) were highly significant, except temperature (E), while for CBZ, only pH (C) and temperature (E) ($p < 0.05$) were found to be significant. The coefficient of the quadratic effect of initial drug concentration ($A \times A$), contact time ($B \times B$), pH ($C \times C$), and adsorbent dose ($D \times D$) were non-significant ($p > 0.05$), except temperature ($E \times E$) ($p < 0.05$) in ASA; however, all the variables were observed to be significant in the case of CBZ. Further, the combined effects of all the variables were observed to be insignificant in ASA. In contrast, for CBZ, the interaction effects, AB, BE, and CD were significant, whereas all other combinations were found to be non-significant ($p > 0.05$). Equations (6) and (7) represents the quadratic model of ASA and CBZ drug removal by BC-CS@nZVI, respectively:

$$\begin{aligned} \text{ASA Removal (\%)} = & 69.52 - 3.45A + 3.32B - 17.12C + 4.59D + 0.047E - 1.32 AB \\ & + 0.28AC - 0.25AD + 0.10AE + 0.75BC - 0.55BD - 0.69BE + 1.26CD - 0.34CE + \\ & 0.42DE - 0.376A^2 - 0.90B^2 - 1.16C^2 - 0.59D^2 + 1.79E^2 \end{aligned} \quad (6)$$

$$\begin{aligned} \text{CBZ Removal (\%)} = & 88.18 - 0.90A + 0.05B + 10.09C + -0.84D + 1.68E + 3.59AB \\ & - 0.81AC - 0.62AD - 1.16AE + 0.36BC - 1.28BD - 1.75BE - 3.21 CD + 0.30 CE \\ & - 4.65 DE - 4.27 A^2 - 2.98 B^2 - 10.35C^2 - 3.31D^2 - 2.76 E^2 \end{aligned} \quad (7)$$

where A, B, C, D, and E represent the drug concentration, contact time, pH, BC-CS@nZVI dose, and temperature, respectively.

The positive coefficient values in the above equation indicate the synergistic impact of independent variables on the removal percentage of ASA and CBZ drugs. In contrast, negative values show that variables have an antagonistic effect on ASA and CBZ removal percentage in the verified range. The high values of R^2 (ASA: 0.9859 and CBZ: 0.9879) and R^2_{adj} (ASA: 0.9602 and CBZ: 0.9658) imply that the selected model is significant and suitable for assuming ASA and CBZ removal (Tables 4 and 5). The R^2_{pred} values of ASA and CBZ were found to be 0.8896 and 0.7698, respectively, showing a high correlation with the R^2_{adj} values. These findings suggest that the selected model for this work is best for predicting ASA and CBZ drug removal percentage over a broad array of parameters.

The low coefficient of variation (CV) percent for both the drugs (ASA: 4.81% and CBZ: 4.02%) indicates that the performed experiments have excellent precision and reliability. The precision ratios of 25.60 for ASA and 26.87 for CBZ further indicate the model's reliability. The predicted residual square sum (PRESS) value for ASA and CBZ removal percentage was 937.06 and 1669.36, respectively. For ASA, the lack of fit (F-value) was 38.36, and in the case of CBZ, it was 44.72. As the F-value was found to be non-significant in the case of both the drugs, it indicates that the employed model was significant.

Table 4. ANOVA results, coefficients of regression, and quadratic summary statistics for the removal of ASA by BC-CS@nZVI obtained by CCD.

Source	Sum of Squares	df	Mean Square	F-Value	p-Value		Regression Coefficient	
Model	8364.66	20	418.23	38.36	<0.0001	significant	Factor	Estimate (ASA)
A-Drug concentration	287.18	1	287.18	26.34	0.0003		Intercept	69.53
B-Contact time	264.40	1	264.40	24.25	0.0005		A-Drug concentration	−3.46
C-pH	7037.69	1	7037.69	645.45	<0.0001		B-Contact time	3.32
D-Adsorbent dose	507.10	1	507.10	46.51	<0.0001		C-pH	−17.12
E-Temperature	0.0545	1	0.0545	0.0050	0.9449		D-Adsorbent dose	4.60
AB	27.83	1	27.83	2.55	0.1385		E-Temperature	0.0477
AC	1.27	1	1.27	0.1161	0.7397		AB	−1.32
AD	1.03	1	1.03	0.0945	0.7643		AC	0.2813
AE	0.1849	1	0.1849	0.0170	0.8987		AD	−0.2537
BC	9.15	1	9.15	0.8392	0.3793		AE	0.1075
BD	5.00	1	5.00	0.4581	0.5125		BC	0.7563
BE	7.78	1	7.78	0.7139	0.4161		BD	−0.5587
CD	25.65	1	25.65	2.35	0.1533		BE	−0.6975
CE	1.90	1	1.90	0.1747	0.6840		CD	1.27
DE	2.82	1	2.82	0.2589	0.6210		CE	−0.3450
A ²	4.16	1	4.16	0.3812	0.5495		DE	0.4200
B ²	24.10	1	24.10	2.21	0.1652		A ²	−0.3764
C ²	39.91	1	39.91	3.66	0.0821		B ²	−0.9064
D ²	10.30	1	10.30	0.9449	0.3519		C ²	−1.17
E ²	94.52	1	94.52	8.67	0.0133		D ²	−0.5927
Residual	119.94	11	10.90				E ²	1.80
Lack of Fit	32.50	6	5.42	0.3098	0.9070	not significant		
Pure Error	87.44	5	17.49					
Cor Total	8484.60	31						
	Mean	Std. Dev.	CV%	PRESS	R ²	Adj. R ²	Pred. R ²	Adeq. precision
	68.59	3.30	4.81	937.06	0.9859	0.9602	0.8896	25.6066

Table 5. ANOVA results, coefficients of regression, and quadratic summary statistics for the removal of CBZ drug by BC-CS@nZVI obtained by CCD.

Source	Sum of Squares	df	Mean Square	F-Value	p-Value		Regression Coefficient	
Model	7163.00	20	358.15	44.72	<0.0001	significant	Factor	Estimate (CBZ)
A-Drug concentration	19.67	1	19.67	2.46	0.1453		Intercept	88.19
B-Contact time	0.0630	1	0.0630	0.0079	0.9309		A-Drug concentration	−0.9054
C-pH	2446.42	1	2446.42	305.48	<0.0001		B-Contact time	0.0512
D-Adsorbent dose	17.32	1	17.32	2.16	0.1694		C-pH	10.10
E-Temperature	68.51	1	68.51	8.56	0.0138		D-Adsorbent dose	−0.8496
AB	206.71	1	206.71	25.81	0.0004		E-Temperature	1.69
AC	10.55	1	10.55	1.32	0.2755		AB	3.59
AD	6.14	1	6.14	0.7664	0.4000		AC	−0.8119
AE	21.69	1	21.69	2.71	0.1280		AD	−0.6194
BC	2.18	1	2.18	0.2726	0.6120		AE	−1.16
BD	26.45	1	26.45	3.30	0.0965		BC	0.3694
BE	49.46	1	49.46	6.18	0.0303		BD	−1.29
CD	165.83	1	165.83	20.71	0.0008		BE	−1.76
CE	1.52	1	1.52	0.1897	0.6716		CD	−3.22
DE	346.24	1	346.24	43.23	<0.0001		CE	0.3081
A ²	535.32	1	535.32	66.84	<0.0001		DE	−4.65
B ²	260.61	1	260.61	32.54	0.0001		A ²	−4.27
C ²	3146.47	1	3146.47	392.89	<0.0001		B ²	−2.98
D ²	322.00	1	322.00	40.21	<0.0001		C ²	−10.36
E ²	223.76	1	223.76	27.94	0.0003		D ²	−3.31
Residual	88.09	11	8.01				E ²	−2.76
Lack of Fit	71.46	6	11.91	3.58	0.0915	not significant		
Pure Error	16.63	5	3.33					
Cor Total	7251.10	31						
	Mean	Std. Dev.	CV%	PRESS	R ²	Adj. R ²	Pred. R ²	Adeq. precision
	70.43	2.83	4.02	1669.36	0.9879	0.9658	0.7698	26.8791

3.2.2. Interaction among Influencing Factors

The optimum level of process variables for obtaining the maximum response was investigated using three-dimensional plots. These plots were produced to visualize the interaction among the independent variables and dependent variables.

Effect of pH and Adsorbent Dose

As the pH affects the solubility, degree of ionization, and surface charge of the nanocomposite, it is considered to be a significant factor [63]. Adsorbent dose, on the other hand, determines the number of active sites available for reaction with the drug molecules. Figure 4 displays the simultaneous influence of pH and the dose of nanocomposite on ASA and CBZ removal efficiency. At a fixed dose of 0.025 g BC-CS@nZVI, ASA removal efficiency was 79.92% at pH 2, while at pH 10, it was reduced up to 8.82% (Figure 4a). At fixed pH 2, when the amount of adsorbent varied from 0.085 to 0.125 g, the ASA displayed 91.20–93.52% removal, showing an increasing trend with the increase in the dose. Similar trends were observed at higher pH values. This specifies that in the case of ASA, the removal efficiency shares an inverse relationship with increasing pH, while the adsorbent dose is directly related to removal efficiency. The relationship of the adsorbent dose is easily understandable, as the increase in the dose leads to an increase in the available active sites, while the changes in the removal efficiency with pH could be explained by the point of zero charge (pH_{pzc}), which was found to be 3.89 for BC-CS@nZVI (Figure 5). When the solution pH was less than pH_{pzc} , the adsorbent surface became protonated with H^+ ions and bore a positive surface charge. ASA species, which are acidic in nature and have a high negative charge density, show greater affinity towards the surface of the nanocomposite at lesser pH due to the abundance of H^+ ions in and around the surface of the nanosorbent, resulting in enhanced removal efficiency. On the contrary, at pH values $> pH_{pzc}$, the adsorbent had a negative charge due to the existence of a large number of OH^- and COO^- ions, eliminating electrostatic attraction between the ASA molecules and the adsorbent, and reducing overall removal efficiency [13]. The results are in accordance with the study conducted by [64], wherein the TiO_2 -mediated photocatalytic degradation rate of aspirin showed an increasing trend with decreasing pH, which is similar to the present study [64]. Similar observations were reported in the study conducted over other acidic drug molecules [65,66].

Similar to the case of ASA, the removal efficiency of CBZ also displayed an accelerating trend with the increase in the dose; however, the influence of pH was different. At a fixed dose, the CBZ removal efficiency was observed to increase up to pH 6, and after that, it remained consistent up to pH 10, as shown in Figure 4f. This indicates that CBZ removal is quite independent of pH, and the increase observed in the removal efficiency up to pH 6 could be the effect of an adsorbent dose. The pK_a value of CBZ could be the reason for the pH independency observed herein. As the pK_a value of CBZ is reported to be 13.9, the molecules of CBZ would have a neutral charge in the studied pH range; therefore, the electrostatic interaction between CBZ and the charged surface of BC-CS@nZVI is not feasible [67,68]. The results are in line with other studies reporting on CBZ removal with AC/ Fe_3O_4 and phenyl-functionalized magnetic palm-based powdered activated carbon adsorbents, wherein pH was varied from 4 to 9 and from 2 to 12, respectively, and the CBZ removal was reported to be unaffected by the solution pH [68,69].

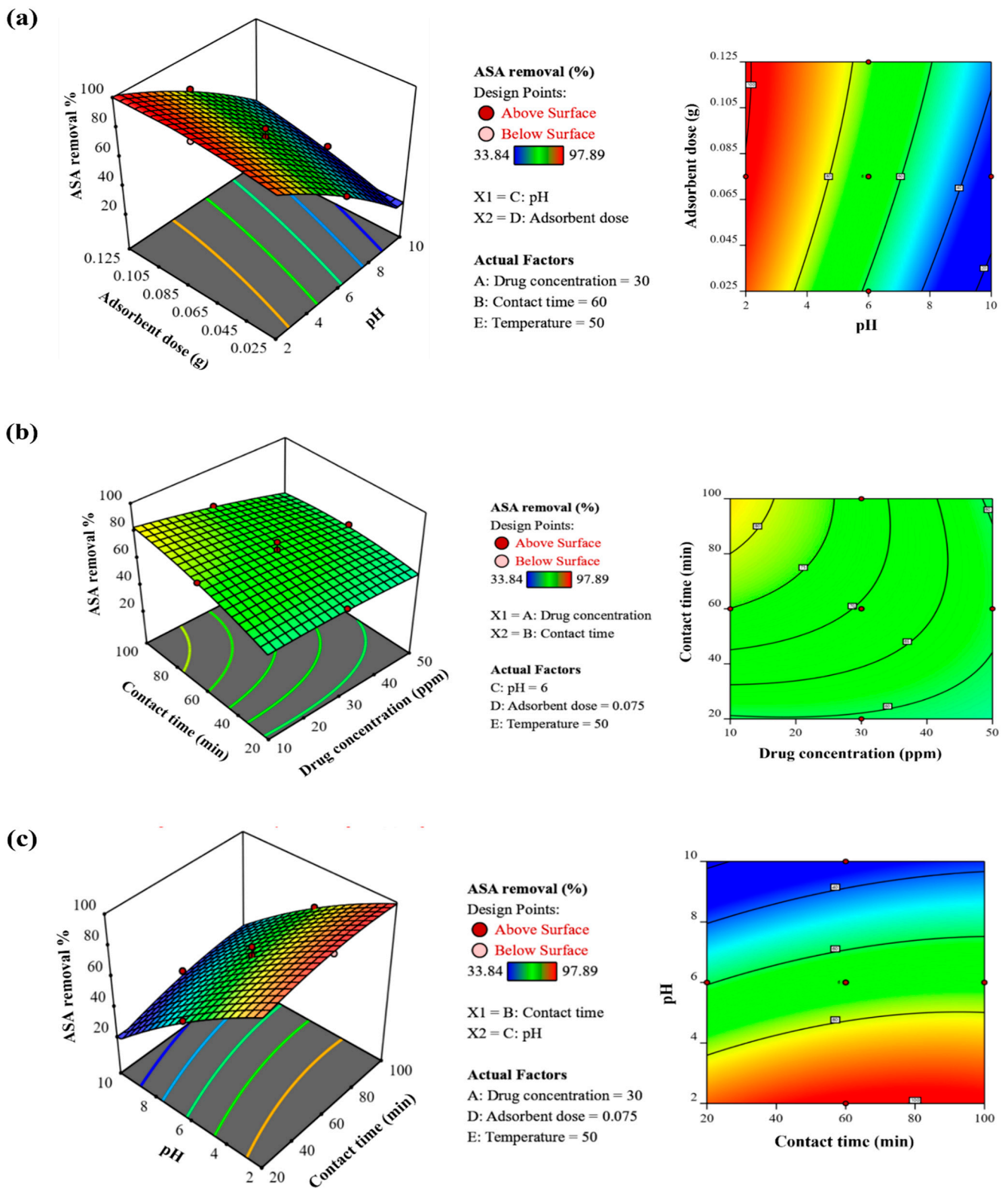


Figure 4. Cont.

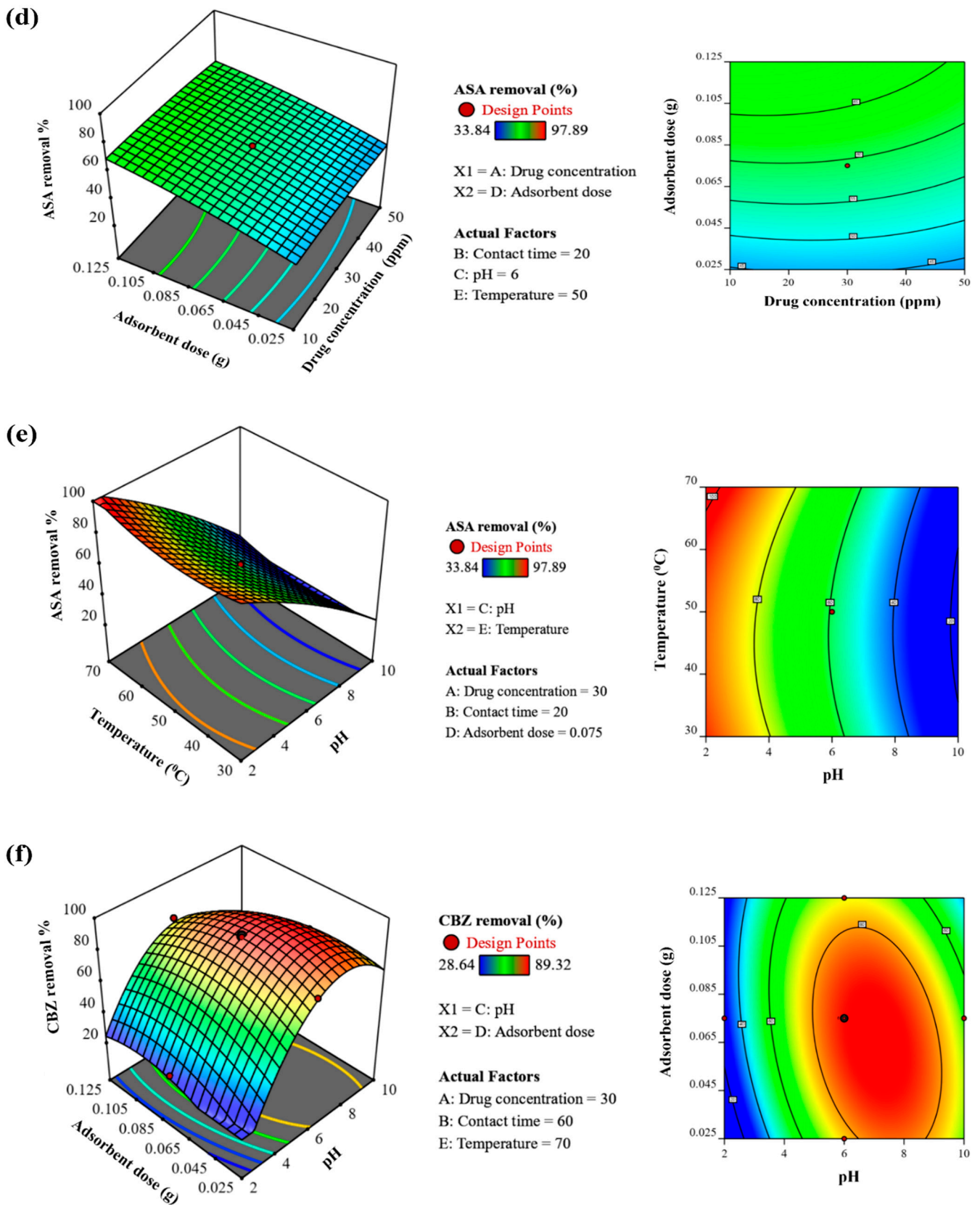


Figure 4. Cont.

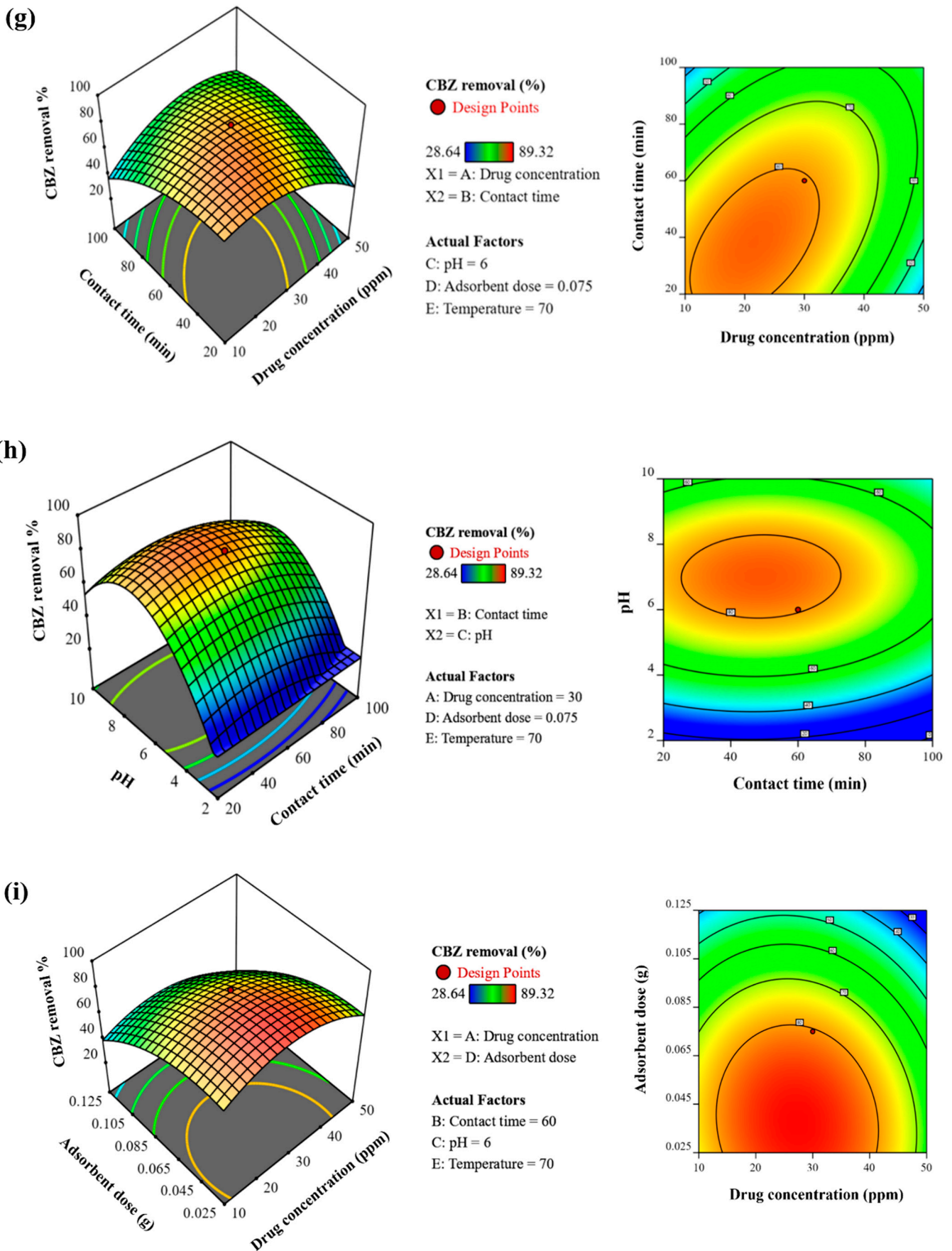


Figure 4. Cont.

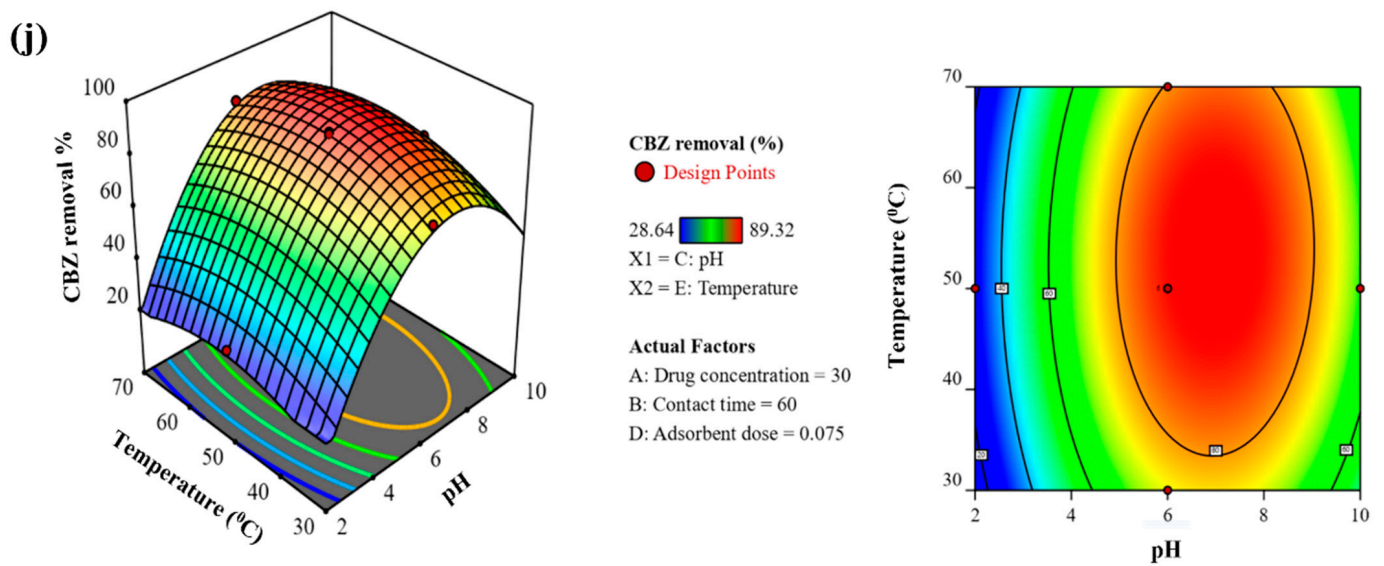


Figure 4. Two-dimensional contour and three-dimensional surface plot for adsorption of ASA and CBZ onto BC-CS@nZVI, showing the interactive effects of: (a,f) Adsorbent dose and pH; (b,g) Contact time and Drug concentration; (c,h): pH and Contact time; (d,i): Adsorbent dose and Drug concentration; (e,j): Temperature and pH.

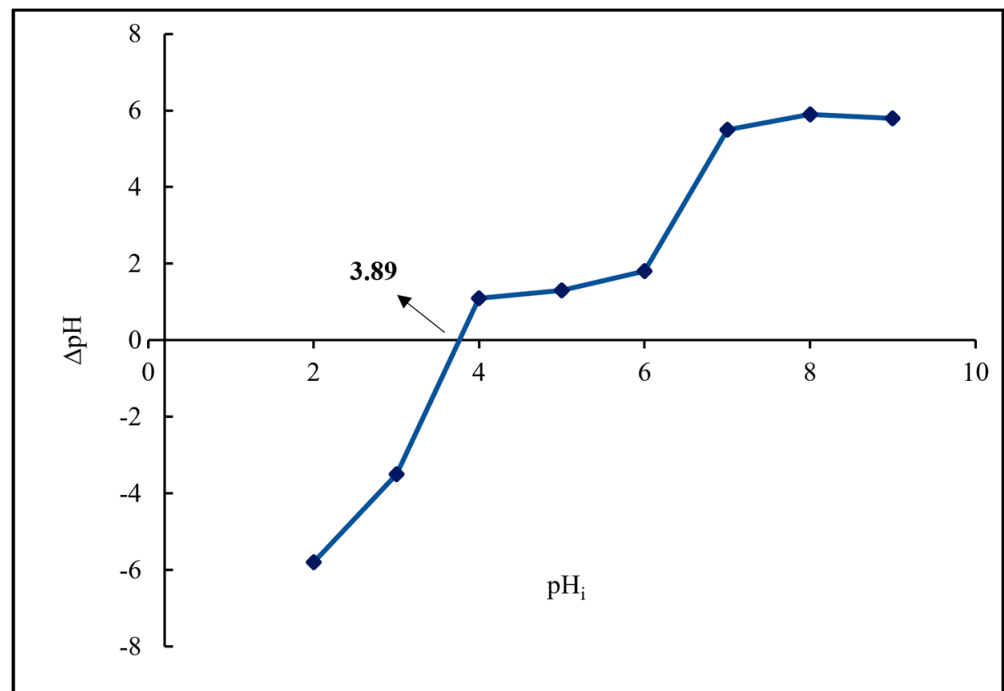


Figure 5. pH_{pzc} value of BC-CS@nZVI nanocomposite.

Effect of Initial Drug Concentration and Contact Time

Figure 4b,g displays the effect of initial drug concentration and contact time on ASA and CBZ removal efficiency. At 30 ppm of ASA and 60 min contact, the maximum removal efficiency of 97.89% was observed, and 88.39% was noticed in CBZ. The removal efficiency was observed to be increasing rapidly during the first 60 min, and after that, no significant changes were noticed. The rapid increase in adsorption capacity noticed in the early phase of the reaction could be due to the abundance of active sites available for adsorption; however, as the time passes, the active sites gradually become saturated and the process

reaches an equilibrium stage [70]. CBZ adsorption onto polypyrrole-chitosan- Fe_3O_4 magnetic nanocomposite (PPy-CS- Fe_3O_4 MNC) and removal of ceftriaxone sodium in aqueous media with novel nanocomposite $\text{g-C}_3\text{N}_4/\text{MWCNT}/\text{Bi}_2\text{WO}_6$ showed similar trends with respect to initial drug concentration and contact time [71,72].

Effect of Contact Time and pH

As shown in Figure 4c,h, along with the increase in the reaction time from 20–100 min, the removal efficiency also became enhanced from 82.57% to 97.89% at lower pH, i.e., 2 for ASA drug, whereas the removal efficiency of CBZ drug at pH 6 increases from 28.64 to 89.32%. The reason for the enhanced adsorption over time could be attributed to increased possibilities of collision between the drug molecules and the adsorbent. A similar result was reported by Yousefi et al. (2021) [73] while studying CIP removal by functionalized multi-walled carbon nanotubes, wherein removal efficiency was boosted up to 88% when contact time was increased up to 24.4 min at pH 5.4.

Effect of Adsorbent Dose and Initial Drug Concentration

Figure 4d,i show the combined effect of adsorbent dose and initial drug concentration. As displayed in the figure, when the drug had an initial concentration of 10 ppm and the adsorbent dose was 0.025 g, the removal efficiency of ASA was 33.84%. At the same concentration level, when the amount of adsorbent dose increased up to 0.125 g, the removal efficiency also increased to 68.56%. Similarly, in the case of CBZ, 28.64% removal was noticed at 10 ppm initial concentration and 0.025 g adsorbent dose, which increased up to 89.32% at 0.125 g of the adsorbent. This indicates that for both the drugs, the removal efficiency is directly proportional to the adsorbent dose and inversely proportional to the drug concentration. Similar results were also reported in other studies [13,74].

Effect of Temperature and pH

Figure 4e,j depict the effects of temperature and pH on the removal efficiency of ASA and CBZ. In the case of both drugs, the rise in temperature coincided with the increase in the removal efficiency. As the temperature increased from 30 °C to 70 °C, maximum removal efficiency of 97.89% ASA and 82.21% CBZ was observed at pH 2 and 6, respectively. The reason could be the increased mobility of drug molecules at higher temperatures, which leads to a greater number of collisions and subsequent adsorption on the surface of BC-CS@nZVI. A similar pattern was observed for CBZ removal by $\text{Co}_3\text{MnFeO}_6$ nanoparticles, wherein a positive relationship between CBZ degradation and elevated temperature was reported. When the temperature was raised to 40 °C, CBZ was removed entirely in 12 min [75,76].

3.2.3. The Diagnostic Plot Analysis

As shown in Figure 6a,b, the data points available on the plots were quite near the straight line, which indicates that the predicted removal percentage of the model matches the experimental removal percentage without outliers and validates the utilized model as accurate and significant. The high order of predictability was confirmed by the random distribution of residuals around the predicted value in both the drugs, as shown in Figure 6c,d. The Cook's distance value lesser than 1 further indicates the excellent predictability and reliability of the model in both cases (Figure 6e,f).

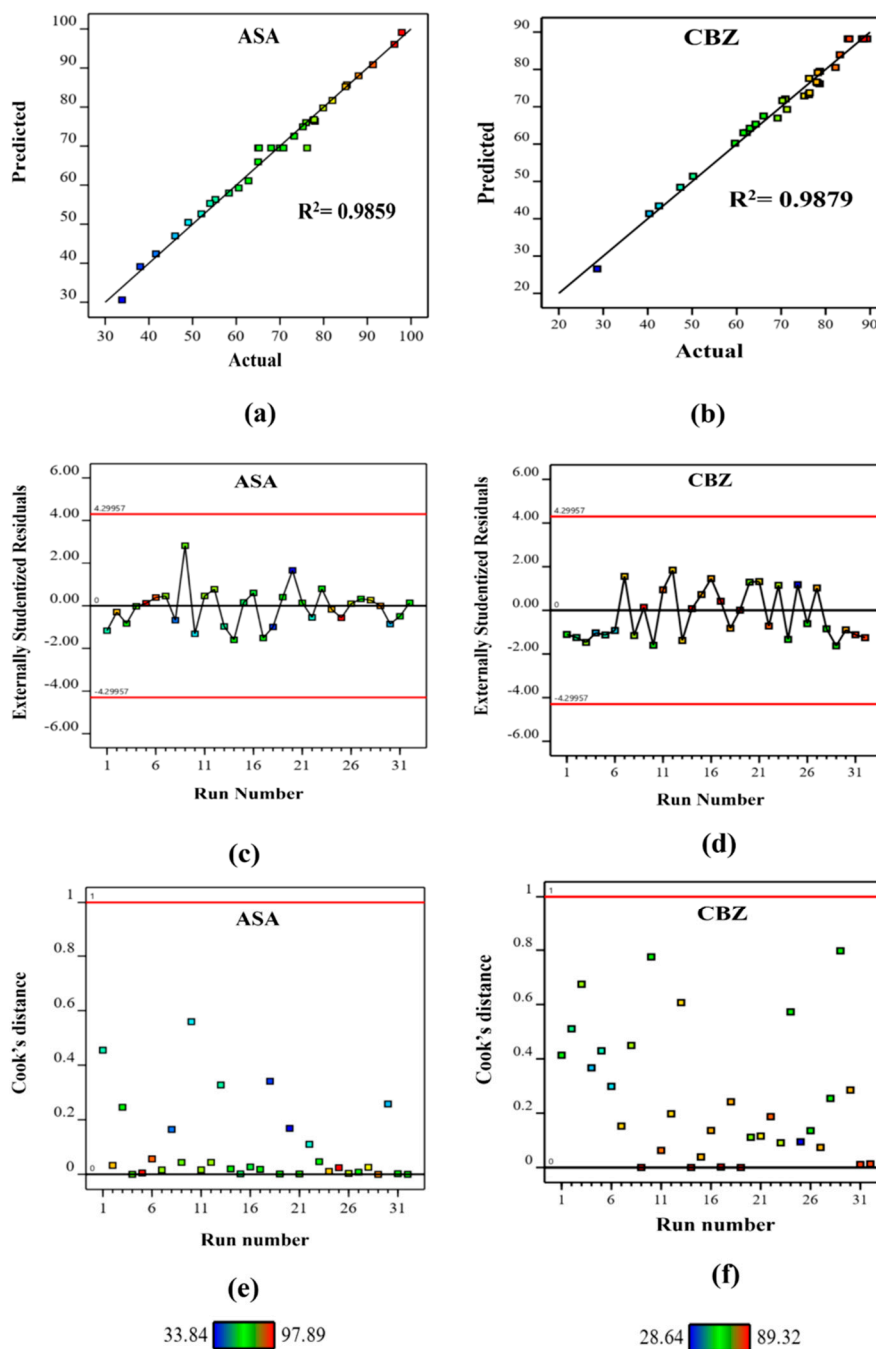


Figure 6. (a,b) Plot of predicted versus actual; (c,d) Residuals versus predicted plot; (e,f) Cook's distance plot versus run number; Box-Cox plot for power transforms plot of ASA and CBZ adsorption onto BC-CS@nZVI.

3.3. Adsorption Kinetic Model

The kinetic studies were performed to explain the adsorption behavior of the nanocomposite for removal of ASA and CBZ using the following models:

3.3.1. Pseudo-First-Order Reaction

The pseudo-first-order kinetic model follows Equation (8) [77,78]:

$$\ln(q_e - q_t) = \ln q_e - k_1 t \tag{8}$$

where q_e and q_t represent the adsorbent capacity (mg/g) (BC-CS@nZVI) at equilibrium and contact time t (min), respectively, and k_1 depicts the velocity coefficients (1/min). The graph plotted between $\ln(q_e - q_t)$ and time t yields values of q_e and k_1 (Figure 7a). The R^2 values for both ASA and CBZ were calculated to be 0.9809 and 0.8006, respectively.

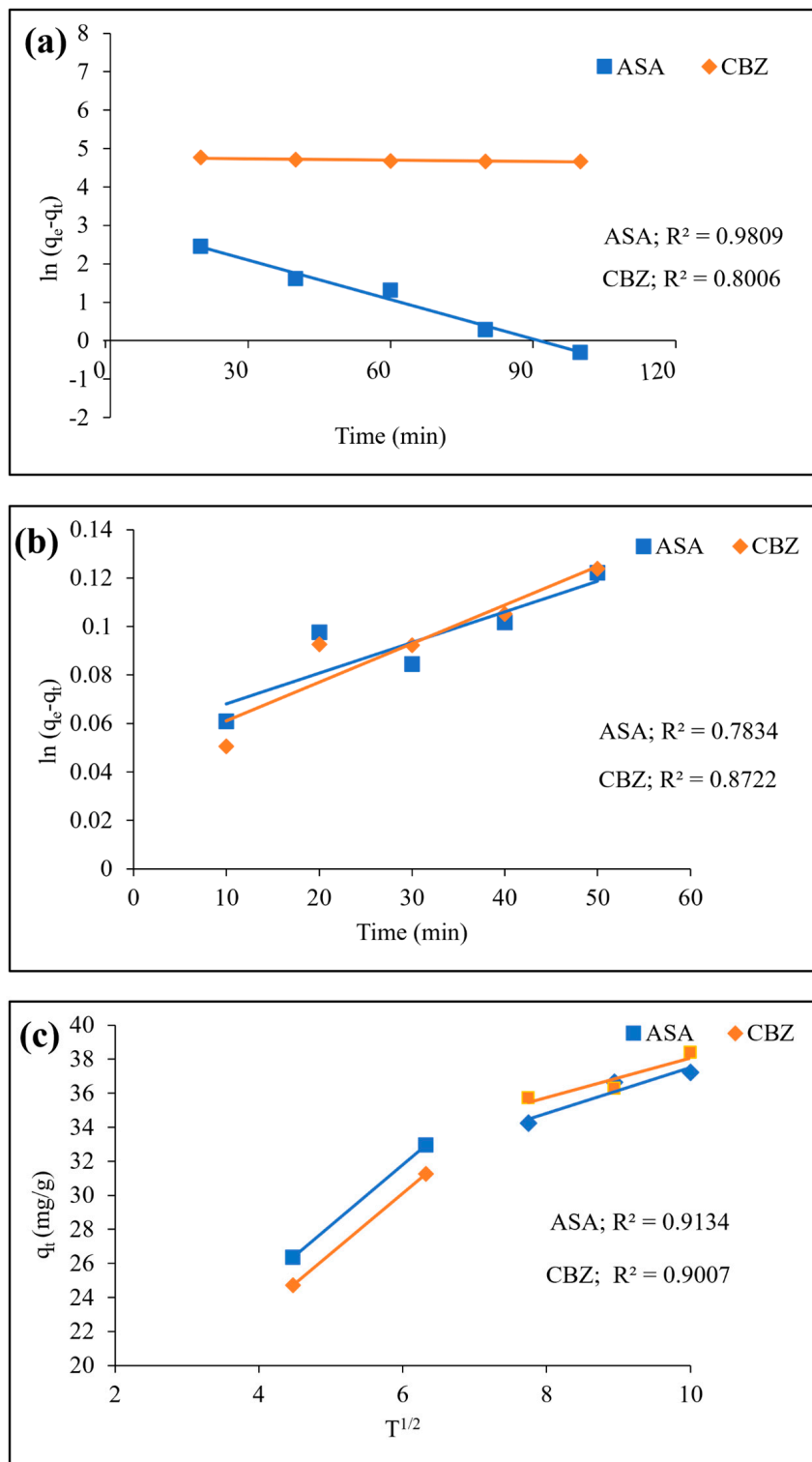


Figure 7. Kinetic models of ASA and CBZ: (a) pseudo-first-order, (b) pseudo-second-order, and (c) intraparticle diffusion.

3.3.2. Pseudo-Second-Order Reaction

The rate equation used to determine the pseudo-second-order reaction kinetics is given below [79,80]:

$$\frac{t}{q_e} = \frac{1}{k_2 q_e^2} + \frac{1}{q_e} \quad (9)$$

where the rate constant is represented by k_2 (mg/g min). The regression coefficient value (R^2) was determined by plotting the graph between t/q_t and t , and it was found to be 0.751 for ASA and 0.8722 for CBZ (Figure 7b).

The above findings indicate that the pseudo-first-order model fits well with the adsorption data of ASA; thus, physisorption is mainly responsible for ASA removal. In contrast, the best-fitted model for CBZ was observed to be the pseudo-second-order reaction model, which indicates that chemisorption is the main mechanism of CBZ removal. Similar observations have also been reported in other studies [70,81].

3.3.3. Intraparticle Diffusion Model

The intraparticle diffusion model is represented in the following equation [82]:

$$q_t = k_i t^{0.5} + C \quad (10)$$

where q_t in mg/g depicts the adsorbate amount adsorbed on the adsorbent surface at time t , C is the value of intercept representing boundary layer effect or surface adsorption, and k_i represents intraparticle rate constant. In the adsorption reaction, intraparticle diffusion between the adsorbate and adsorbent is regarded as the primary rate-controlling step if the plot of target molecules adsorbed against $t^{1/2}$ yields a straight line. In the present study, two-phase plots were observed for both the drugs, as shown in Figure 7c. The first phase of the curve shows the external mass transfer of the ASA and CBZ from the solution to the surface of BC-CS@nZVI, while the second phase displays intraparticle diffusion occurring on the BC-CS@nZVI nanocomposite. In the case of ASA, the intraparticle diffusion rate constant (k_i) is higher, while the intercept C , representing the boundary layer effect, is lower, signifying that in ASA, diffusion is the major rate-controlling step; thus, the removal kinetics is controlled by physisorption. In contrast, k_i and C values of CBZ indicate that the surface adsorption was comparatively higher, lowering the surface diffusion of the CBZ molecules from the external surface of the adsorbent to its internal surface, indicating chemisorption as the major rate-controlling step. These results are in agreement with the kinetic data obtained for ASA and CBZ removal. As the linear segments in neither graph plotted between q_t and $t^{1/2}$ for the intraparticle diffusion model pass through the origin, this indicates that intraparticle diffusion is not the only rate-controlling step; there are additional kinetic processes, such as boundary layer effects, which regulate the adsorption rate [77,83]. Table 6 displays the kinetic model parameters discussed above.

Table 6. Kinetic parameters for ASA and CBZ adsorption onto BC-CS@nZVI.

S.No.	Kinetics Parameters	Values	
		ASA	CBZ
1.	Pseudo-first-order	$q_e \text{ max (Cal)} = 22.79 \text{ mg/g}$	$q_e \text{ max (Cal)} = 118.63 \text{ mg/g}$
		$q_e \text{ max (exp)} = 37.95 \text{ mg/g}$	$q_e \text{ max (exp)} = 142.28 \text{ mg/g}$
2.	Pseudo-second-order	$K_1 = -0.0005$	$K_1 = -2.17$
		$R^2 = 0.9809$	$R^2 = 0.8006$
		$q_e \text{ max (Cal)} = 769.23 \text{ mg/g}$	$q_e \text{ max (Cal)} = 625 \text{ mg/g}$
		$q_e \text{ max (exp)} = 37.95 \text{ mg/g}$	$q_e \text{ max (exp)} = 142.28 \text{ mg/g}$
3.	Intraparticle diffusion	$q_e^2 = 591716$	$q_e^2 = 390625$
		$K_2 = 0.0013$	$K_2 = 5.66$
		$R^2 = 0.751$	$R^2 = 0.8722$
		$k_i = 1.3425 \text{ g/mg min}$	$k_i = 0.2946 \text{ g/mg min}$
		$C = 24.08$	$C = 35.50$
		$R^2 = 0.9134$	$R^2 = 0.9007$

3.4. Thermodynamic Study

The thermodynamic parameters were calculated using the following equations [84] and are represented in Table 7.

$$\ln K = \frac{\Delta S^\theta}{R} - \frac{\Delta H^\theta}{RT} \quad (11)$$

$$\Delta G^\theta = -RT \ln K \quad (12)$$

where R depicts the universal gas constant ($8.314 \text{ J mol}^{-1}\text{K}^{-1}$), the equilibrium constant is K , and T represents the absolute temperature, as shown in Figure 8. In the temperature range of 303 K to 343 K, the calculated ΔG^θ value for ASA adsorption was found to be -0.44 to -1.06 , and for CBZ, it was -0.04 to -5.14 kJ/mol. The negative values of ΔG^θ confirm the spontaneity and feasibility of the reaction. The value of ΔH^θ for ASA and CBZ was calculated as -0.073 and -0.003 kJ/mol, which validates the exothermic nature of the adsorption reaction. The change in entropy (ΔS^θ) was -0.011 and -0.004 kJ/mol for ASA and CBZ, which corresponds to a decrease in the degree of randomness of the adsorbate at solid–liquid interface during the reaction.

Table 7. The thermodynamic parameters of ASA and CBZ adsorption onto BC-CS@nZVI.

PhAC	Temperature (K)	$-\Delta G^\theta$ (kJ/mol)	ΔS^θ (kJ/mol)	ΔH^θ (kJ/mol)
ASA	303	-0.44228	-0.01125	-0.0035
	313	-2.21769		
	323	-4.28489		
	333	-9.96554		
	343	-1.06059		
CBZ	303	-0.04208	-0.00498	-0.0735
	313	-1.43613		
	323	-3.0971		
	333	-4.74838		
	343	-5.14778		

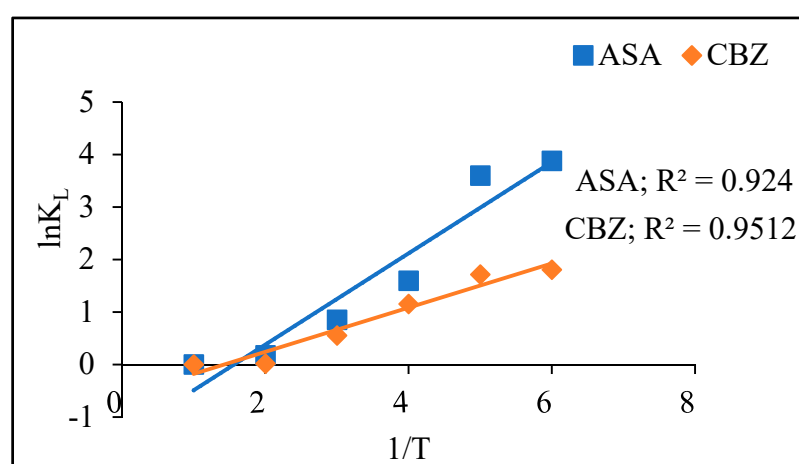


Figure 8. Thermodynamic parameters for ASA and CBZ adsorption.

3.5. Adsorption Isotherms

The adsorption isotherm is a frequently used technique which can help to understand the adsorption mechanism, surface properties, and the affinity between adsorbate and adsorbent. In addition, it provides a description of the adsorbent's capability [85]. In the present study,

three isotherm models, viz. Langmuir, Freundlich, and Temkin isotherms, were used to determine the maximum adsorption capacity of the adsorbent and the process viability.

3.5.1. Langmuir Isotherm

The Langmuir isotherm is based on several hypotheses, including monolayer adsorption and similarity in the energy of the active sites [86]. The following equation describes the Langmuir isotherm model:

$$\frac{1}{q_e} = \frac{1}{K_L q_{max}} \times \frac{1}{C_e} + \frac{1}{q_{max}} \quad (13)$$

where C_e depicts the concentration of drugs at equilibrium (ppm), q_e (mg/g) is the adsorbent's maximum adsorption capacity, q_{max} (mg/g) explains the theoretical maximum adsorption capacity, and K_L (L/mg) depicts the Langmuir adsorption constant. The graph plotted between C_e/q_e and C_e gives the value of q_{max} , and K_L was obtained by the intercept and slope of the linear equation. As displayed in Figure 9a,b, the Langmuir isotherm model fitted well for both ASA and CBZ adsorption data, with R^2 values of 0.7502 and 0.926, respectively, indicating that the active sites are evenly distributed on the surface of the nanocomposite, showing monolayer sorption of both the drugs over BC-CS@nZVI. The q_e of BC-CS@nZVI for ASA and CBZ drug removal was calculated as 20.62 mg/g and 55.24 mg/g, respectively.

3.5.2. Freundlich Isotherm

The Freundlich isotherm describes mainly multilayer adsorption of the adsorbate on the non-uniform, or heterogeneous, surface of the adsorbent (Equation (14)).

$$\log q_e = \log K_f + \frac{1}{n} \log C_e \quad (14)$$

where K_f (L mg⁻¹) demonstrates the Freundlich isotherm constants, and $1/n$ describes the intensity of the heterogeneity factor [87]. The graph plotted between $\log C_e$ and $\log q_e$ was used to calculate the value of n , and K_f was obtained using the slope and intercept of the straight-line equation, as shown in Figure 9b. The low value of R^2 specifies that the experimental data of neither drug fit the Freundlich isotherm model, eliminating the probability of multilayer adsorption of ASA and CBZ over BC-CS@nZVI.

3.5.3. Temkin Isotherm

As per the Temkin model, the adsorption heat of surface molecules or particles varies linearly and not in a coverage-dependent manner. The following equation explains this model isotherm:

$$q_e = B_T \ln(A_T) + B_T \ln(C_e) \quad (15)$$

where $B_T = R_T/b_T$, A_T is expressed as the Temkin isotherm equilibrium binding constant (L/g), B_T depicts the constant value of the heat of adsorption (kJ/mol), and R represents the universal gas constant (8.314 J/mol/K). The experimental data of neither drug fit well, with low R^2 values of 0.39 and 0.73, respectively (Figure 9c). The values of isotherm models are summarized in Table 8.

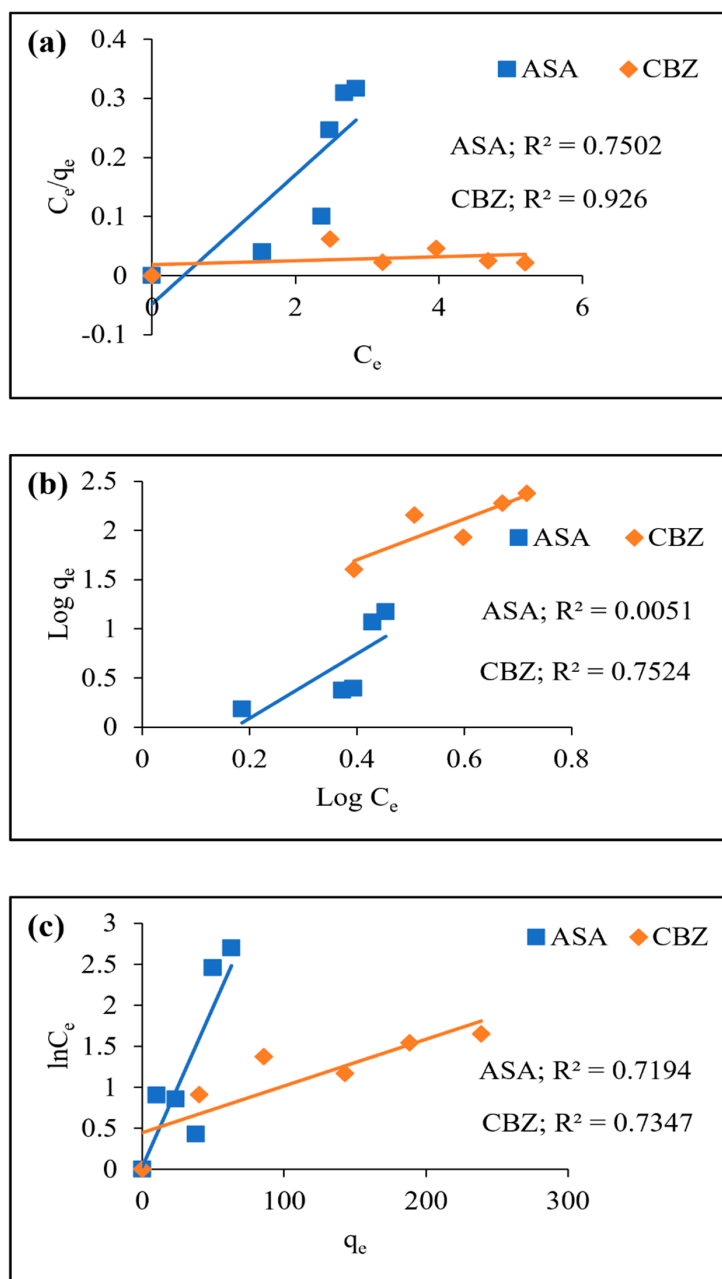


Figure 9. Adsorption isotherms of ASA and CBZ drugs: (a) Langmuir isotherm, (b) Freundlich isotherm, and (c) Temkin isotherm.

Table 8. Adsorption isotherm parameters for ASA and CBZ adsorption onto BC-CS@nZVI.

S.No.	Isotherm Parameter	Values	
		ASA	CBZ
1.	Langmuir Isotherm	$K_L = 0.442 \text{ L/mg}$	$K_L = 5.171 \text{ L/mg}$
		$q_{\max} = 20.62 \text{ mg/g}$	$q_{\max} = 55.25 \text{ mg/g}$
		$R_L = 0.008$	$R_L = 0.101$
		$R^2 = 0.7502$	$R^2 = 0.926$
2.	Freundlich Isotherm	$1/n = 0.212$	$1/n = 2.072$
		$K_f = 25.81 \text{ L/mg}$	$K_f = 7.46 \text{ L/mg}$
		$R^2 = 0.0051$	$R^2 = 0.7524$
3.	Temkin Isotherm	$B_T = 0.0107 \text{ (J/mol)}$	$B_T = 0.0057 \text{ (J/mol)}$
		$A_T = 1.894 \text{ (L/mol)}$	$A_T = 9.094 \text{ (L/mol)}$
		$R^2 = 0.3927$	$R^2 = 0.7347$

3.6. Reusability of BC-CS@nZVI

The reusability of the adsorbent is one among the significant attributes for the practical and cost-effective application of the adsorbent. In the present study, the adsorption/removal efficiency of BC-CS@nZVI in five cycles was found to be in the range of 96–54% and 87–44%, while desorption varied within 90–47% and 80–40% in ASA and CBZ, respectively (Figure 10). This finding indicates that the synthesized nanocomposite bears good stability. In addition, the magnetic property of the BC-CS@nZVI, which facilitates the easy and efficient separation of the nanocomposites while minimizing their loss after each cycle, could have further contributed towards the retention of good removal efficiencies.

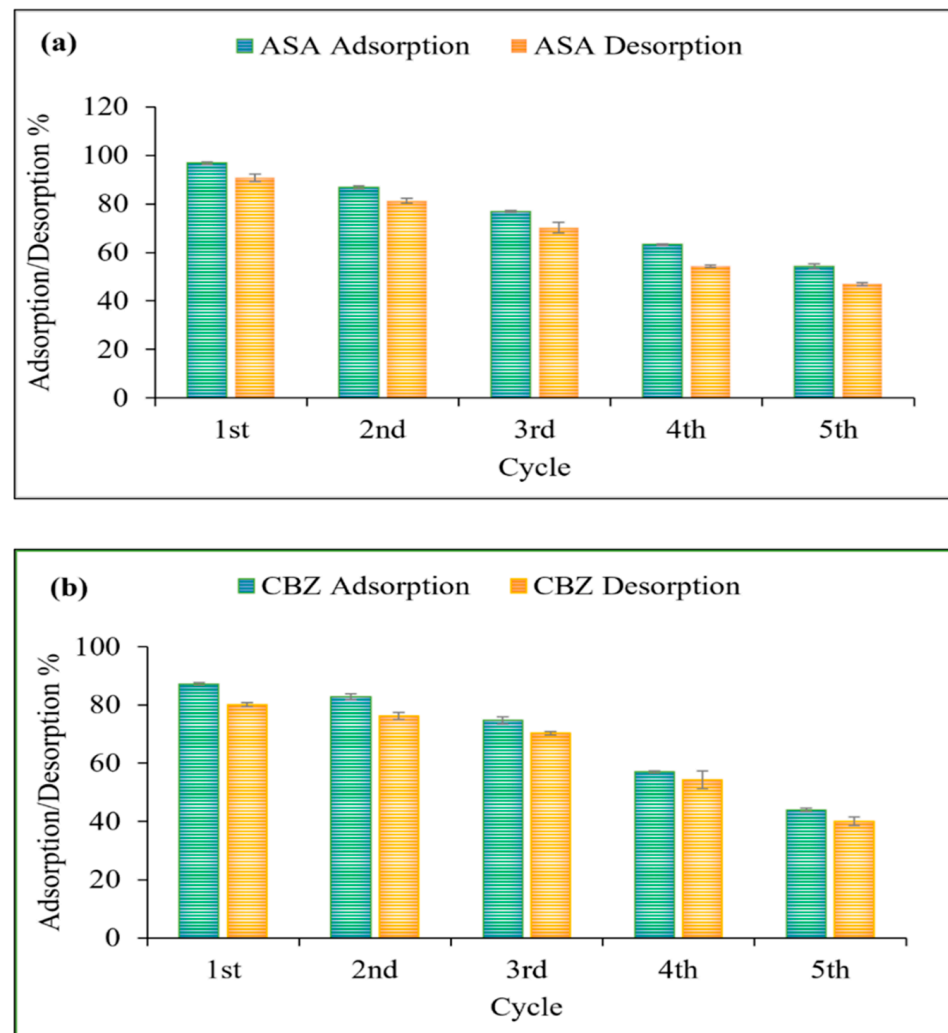


Figure 10. Reusability of BC-CS@nZVI: (a) ASA adsorption/desorption percentage and (b) CBZ adsorption/desorption percentage.

3.7. Comparison with Other Adsorbents

The comparison of the removal efficiency of different adsorbents with the prepared nanocomposite for ASA and CBZ are summarized in Table 9. It could be seen here that the removal percent of the nanocomposite (BC-CS@nZVI) reported in the present work has better efficiency in comparison with other adsorbents, such as pinewood-derived nano biochar, bimetallic nano zero-valent Fe/Cu, granular carbon nanotubes (CNTs)/alumina (Al₂O₃) hybrid, and various other nanoparticles or nanocomposites for similar drug molecules. This signifies that BC-CS@nZVI bears great potential as a remediation agent and could be further explored for the removal of other categories of pollutants.

3.8. Application in Real Water Samples

The results reveal that even in real water samples, BC-CS@nZVI has excellent removal efficiency. In tap water, the maximum removal efficiency was found to be 81.6% and 87.5% for ASA and CBZ, respectively, while in sewage samples, it was 69.8% and 58.2% for ASA and CBZ drugs, respectively. The difference observed between the tap water, and sewage is obvious, as the sewage water would have a high concentration of impurities, which compete with target contaminants for the active locations of BC-CS@nZVI, resulting in relatively lower removal efficiency [88]. This finding implies that the BC-CS@nZVI nanocomposite has a high potential for drug removal, making it a viable candidate for a wide range of applications in real samples.

3.9. Mechanisms of ASA and CBZ Removal by BC-CS@nZVI

Based on the isotherm and kinetic studies, the possible mechanism of the interaction between the surface of BC-CS@nZVI and the drug molecules has been explained below and elucidated in Figure 11a,b.

I. Hydrogen bonding is a potential interaction that could occur between drug molecules and the nanocomposite (BC-CS@nZVI). The carboxylic group in ASA, having an oxygen and amide group in CBZ-containing oxygen/nitrogen, could form hydrogen bonds with the free hydrogen and hydroxyl groups present on the surface of the composite [89–92].

II. π - π interactions could also be a probable mechanism. In ASA, the carbon/hydrogen-containing benzene ring and carboxylic group of ASA could serve as a π -electron acceptor. Similarly, in the case of CBZ, the amino functional groups and oxygen/nitrogen-containing hetero aromatic ring serve as π -electron acceptors. The dominating functional groups, such as -OH, C=O, and C=C present on the surface of BC-CS@nZVI act as a π -electron donor. This causes electrostatic attraction between the positively charged CBZ due to cationic amino groups present on its surface and negatively charged BC-CS@nZVI surface due to the hydroxyl and carboxyl group, whereas in ASA, adsorption is controlled by weak interaction between molecules due to negative charges on both the surface of adsorbate and adsorbent [40,93].

III. Another mechanism could be pore filling, which is basically a physical process wherein small-size ASA molecules diffuse into the meso/macro pores of the adsorbent [88].

IV. Another possible mechanism may be Lewis's acid–base interaction, where NH_2 of CBZ functions as Lewis's base, and oxygen-containing groups present in BC-CS@nZVI act as Lewis's acid [94,95].

Table 9. Comparative study of different adsorbents with the present study.

S.No.	Adsorbent	Adsorbate	Adsorption Capacity (mg/g or R%)	References
1.	Pinewood-derived nano biochar	CBZ	74 $\mu\text{g/g}$	[90]
2.	Bimetallic nano zero-valent Fe/Cu	CBZ	26.15	[92]
3.	Granular carbon nanotubes (CNTs)/alumina (Al_2O_3) hybrid	CBZ	157.4 $\mu\text{mol/g}$	[93]
4.	UiO-66 (Universitetet i Oslo)// Graphene nanoplatelet (GNP)/UiO-66 composites	CBZ	16.69 mg/g/ 51.17 mg/g	[7]
5.	Upconversion particles (UCNPs@MIP) coated with new molecular-imprinted polymer	CBZ	2.23 mg/g	[14]
6.	UV/ZnO	ASA	83.11%	[13]
7.	Magnetite nanoparticle immobilization on a carbon felt cathode	ASA	94.3%	[12]
8.	500 °C-calcinated nanosheets (TiO_2 -BNSs-500)	ASA	87.8%	[5]
9.	Rice hull activated carbon	ASA	95.42%	[66]
10.	Graphene nanoplatelets	ASA	94.3%	[95]
11.	Biochar-supported chitosan-modified nanoscale zero-valent iron (BC-CS@nZVI)	ASA CBZ	97.8% (20.62 mg/g) 89.32% (55.25 mg/g)	Present study

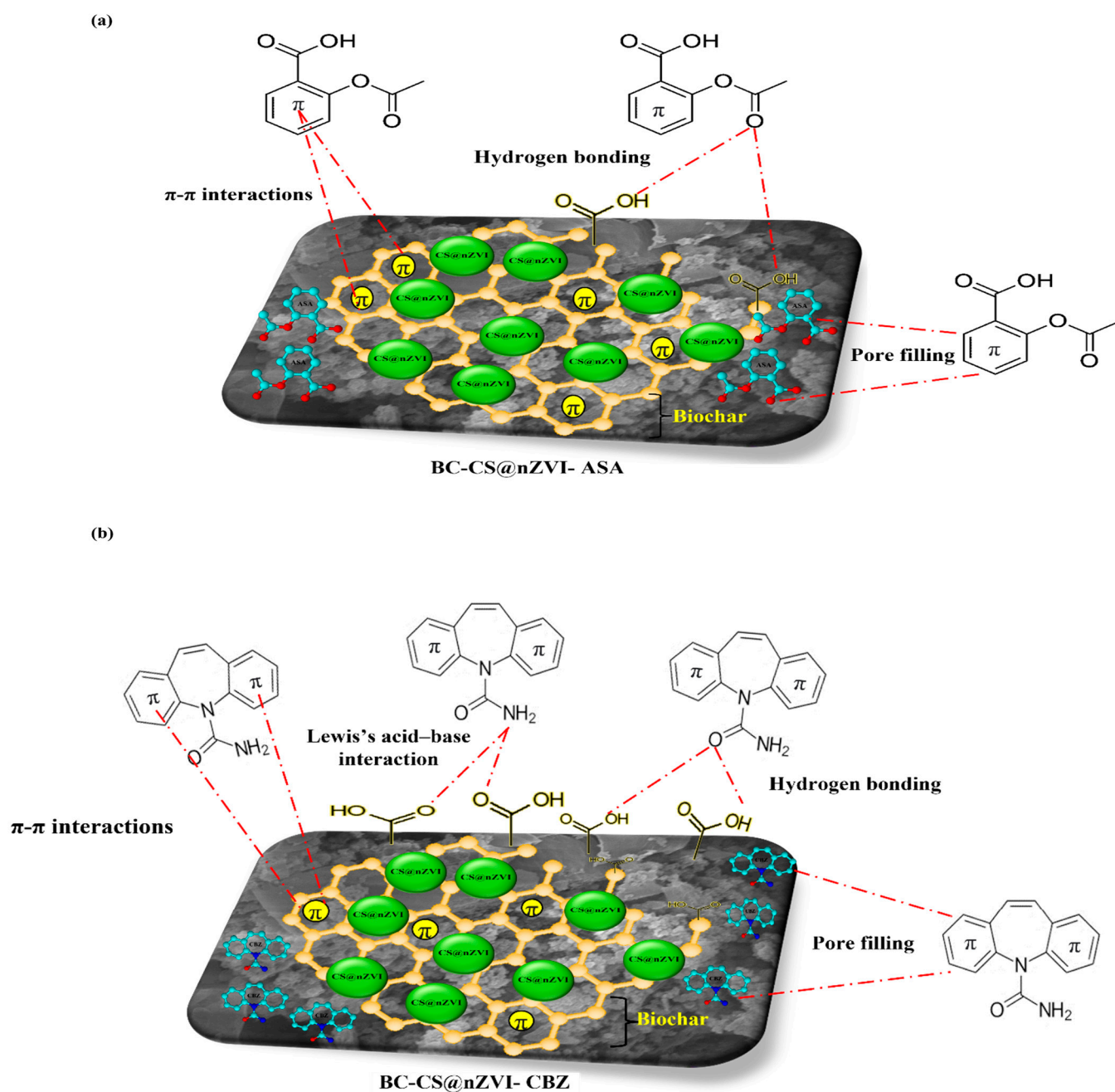


Figure 11. Possible ways of interactions between (a) BC-CS@nZVI and ASA drug molecules and (b) BC-CS@nZVI and CBZ drug molecules.

To sum up, the adsorption mechanisms of the two drugs onto BC-CS@nZVI were relatively similar. They include hydrogen bonding, pore filling, π - π interactions, and Lewis's acid–base interaction; however, based on the structure and properties of the drug, the contribution of all the mechanisms during the adsorption process could be different.

4. Conclusions

In the present study, a simple wet reduction method was used for the synthesis of a magnetic nanocomposite of sugarcane-bagasse-based biochar, chitosan, and nZVI nanoparticles (BC-CS@nZVI), which was employed as an adsorbent for the removal of two PhACs, i.e., aspirin (ASA) and carbamazepine (CBZ), from aqueous solution. The as-synthesized nanocomposite was characterized with XRD, FTIR, SEM, and EDX. The results

of XRD and FTIR were found to be in agreement with SEM and EDX results, confirming the presence of biochar, chitosan, and nZVI nanoparticles in the synthesized nanocomposite. RSM-CCD model was employed to optimize and examine the effects of various process parameters. The quadratic model was found to be the most suitable model to provide an adequate prediction of ASA and CBZ removal efficiency. The experimental results showed maximum removal efficiency of 97.89% for ASA and 89.32% for CBZ under optimized conditions, viz. initial drug concentration: 30 ppm, adsorbent dose: 0.075 g, time: 60 min, temperature: 50 °C, and pH:2 for ASA and pH:6 for CBZ. The adsorption of ASA fitted well with the pseudo-first-order kinetic model, indicating physisorption as the major rate-controlling step, while CBZ adsorption agreed with the pseudo-second-order kinetic model, demonstrating chemisorption as the major rate-controlling mechanism. The isotherm data for ASA and CBZ fitted well with the Langmuir reaction model, showing monolayer adsorption on the surface of BC-CS@nZVI. The thermodynamic parameters revealed the spontaneous and exothermic nature of the adsorption process. In addition, BC-CS@nZVI exhibited good reusability and applicability in real water matrices of the Ha'il region. The fast reaction kinetics and easy magnetic separation of BC-CS@nZVI suggest that it could be employed as an efficient, economical, and environmentally friendly alternative for the remediation of PhACs-contaminated water. Further, the conversion of agro-waste hazard into highly efficient adsorbent paves the way for future research for utilizing biomass waste in environmental remediation.

Author Contributions: Conceptualization, A.J.S. and R.S.; methodology, J.S., A.A., N.K. and M.S.; validation, M.S., A.A., J.S., M.A., R.B. and P.K.; formal analysis, M.A., R.B., P.K., A.A., S.K. and N.K.; investigation, S.K., R.B., J.S., P.K., M.S., A.A. and A.J.S.; data curation, R.S., M.A., M.S., J.S., P.K. and R.B.; writing—original draft preparation, A.J.S., R.S. and N.K.; writing—review and editing, A.J.S., R.S. and P.K.; visualization, A.A., J.S., M.S. and R.B.; supervision, A.J.S. and R.S.; project administration, A.J.S. All authors have read and agreed to the published version of the manuscript.

Funding: This research was funded by Scientific Research Deanship at the University of Ha'il–Saudi Arabia through project number RD-21090.

Data Availability Statement: The authors confirm that the data supporting the findings of this study are available within the article.

Acknowledgments: The authors would like to acknowledge all the support and technical assistance provided by the Scientific Research Deanship at the University of Ha'il–Saudi Arabia through project number RD-21090.

Conflicts of Interest: The authors declare no conflict of interest.

References

1. Ebele, A.J.; Abou-Elwafa Abdallah, M.; Harrad, S. Pharmaceuticals and personal care products (PPCPs) in the freshwater aquatic environment. *Emerg. Contam.* **2017**, *3*, 1–16. [[CrossRef](#)]
2. Karimi-Maleh, H.; Ayati, A.; Davoodi, R.; Tanhaei, B.; Karimi, F.; Malekmohammadi, S.; Orooji, Y.; Fu, L.; Sillanpää, M. Recent advances in using of chitosan-based adsorbents for removal of pharmaceutical contaminants: A review. *J. Clean. Prod.* **2021**, *291*, 125880. [[CrossRef](#)]
3. Ma, N.; Liu, X.W.; Yang, Y.J.; Li, J.Y.; Mohamed, I.; Liu, G.R.; Zhang, J.Y. Preventive Effect of Aspirin Eugenol Ester on Thrombosis in κ -Carrageenan-Induced Rat Tail Thrombosis Model. *PLoS ONE* **2015**, *10*, e0133125. [[CrossRef](#)] [[PubMed](#)]
4. Adebayo, G.I.; Williams, J.; Healy, S. Aspirin esterase activity—Evidence for skewed distribution in healthy volunteers. *Eur. J. Intern. Med.* **2007**, *18*, 299–303. [[CrossRef](#)] [[PubMed](#)]
5. Li, D.; Cheng, X.; Yu, X.; Xing, Z. Preparation and characterization of TiO₂-based nanosheets for photocatalytic degradation of acetylsalicylic acid: Influence of calcination temperature. *Chem. Eng. J.* **2015**, *279*, 994–1003. [[CrossRef](#)]
6. Gierbolini, J.; Giarratano, M.; Benbadis, S.R. Carbamazepine-related antiepileptic drugs for the treatment of epilepsy—a comparative review. *Expert Opin. Pharmacother.* **2016**, *17*, 885–888. [[CrossRef](#)] [[PubMed](#)]
7. ElHusseini, E.A.A.; Şahin, S.; Bayazit, Ş.S. Removal of carbamazepine using UiO-66 and UiO-66/graphene nanoplatelet composite. *J. Environ. Chem. Eng.* **2020**, *8*, 103898. [[CrossRef](#)]
8. Almeida, C. Overview of Sample Preparation and Chromatographic Methods to Analysis Pharmaceutical Active Compounds in Waters Matrices. *Separations* **2021**, *8*, 16. [[CrossRef](#)]

9. Clara, M.; Strenn, B.; Kreuzinger, N. Carbamazepine as a possible anthropogenic marker in the aquatic environment: Investigations on the behaviour of Carbamazepine in wastewater treatment and during groundwater infiltration. *Water Res.* **2004**, *38*, 947–954. [[CrossRef](#)]
10. Ginebreda, A.; Muñoz, I.; de Alda, M.L.; Brix, R.; López-Doval, J.; Barceló, D. Environmental risk assessment of pharmaceuticals in rivers: Relationships between hazard indexes and aquatic macroinvertebrate diversity indexes in the Llobregat River (NE Spain). *Environ. Int.* **2010**, *36*, 153–162. [[CrossRef](#)]
11. Vieno, N.M.; Härkki, H.; Tuhkanen, T.; Kronberg, L. Occurrence of pharmaceuticals in river water and their elimination in a pilot-scale drinking water treatment plant. *Environ. Sci. Technol.* **2007**, *41*, 5077–5084. [[CrossRef](#)] [[PubMed](#)]
12. Muzenda, C.; Arotiba, O.A. Improved Magnetite Nanoparticle Immobilization on a Carbon Felt Cathode in the Heterogeneous Electro-Fenton Degradation of Aspirin in Wastewater. *ACS Omega* **2022**, *7*, 19261–19269. [[CrossRef](#)] [[PubMed](#)]
13. Karimi, P.; Baneshi, M.M.; Malakootian, M. Photocatalytic degradation of aspirin from aqueous solutions using the UV/ZnO process: Modelling, analysis and optimization by response surface methodology (RSM). *Desalination Water Treat.* **2019**, *161*, 354–364. [[CrossRef](#)]
14. Elmasry, M.R.; Tawfik, S.M.; Kattaev, N.; Lee, Y.-I. Ultrasensitive detection and removal of carbamazepine in wastewater using UCNPs functionalized with thin-shell MIPs. *Microchem. J.* **2021**, *170*, 106674. [[CrossRef](#)]
15. Liu, K.; Yu, J.C.-C.; Dong, H.; Wu, J.C.S.; Hoffmann, M.R. Degradation and Mineralization of Carbamazepine Using an Electro-Fenton Reaction Catalyzed by Magnetite Nanoparticles Fixed on an Electro-catalytic Carbon Fiber Textile Cathode. *Environ. Sci. Technol.* **2018**, *52*, 12667–12674. [[CrossRef](#)]
16. Ngeno, E.C.; Mbuci, K.E.; Necibi, M.C.; Shikuku, V.O.; Olisah, C.; Ongulu, R.; Matovu, H.; Ssebugere, P.; Abushaban, A.; Sillanpää, M. Sustainable re-utilization of waste materials as adsorbents for water and wastewater treatment in Africa: Recent studies, research gaps, and way forward for emerging economies. *Environ. Adv.* **2022**, *9*, 100282. [[CrossRef](#)]
17. Kyzas, G.Z.; Kostoglou, M. Green Adsorbents for Wastewaters: A Critical Review. *Materials* **2014**, *7*, 333–364. [[CrossRef](#)]
18. Dai, Y.; Sun, Q.; Wang, W.; Lu, L.; Liu, M.; Li, J.; Yang, S.; Sun, Y.; Zhang, K.; Xu, J.; et al. Utilizations of agricultural waste as adsorbent for the removal of contaminants: A review. *Chemosphere* **2018**, *211*, 235–253. [[CrossRef](#)]
19. Sulyman, M.; Namiesnik, J.; Gierak, A. Low-cost Adsorbents Derived from Agricultural By-products/Wastes for Enhancing Contaminant Uptakes from Wastewater: A Review. *Pol. J. Environ. Stud.* **2017**, *26*, 479–510. [[CrossRef](#)]
20. Mpatani, F.M.; Kombo, U.M.; Kheir, K.R.; Nassor, N.K.; Joshua, D.; Mussa, S.S.; Mohamed, S.A.; Mbarak, S.A.; Hamad, A.S.; Ahmada, S.A. Impregnation of Silver Nanoparticles onto Polymers Based on Sugarcane Bagasse for the Remediation of Endocrine Disruptor-Bisphenol A from Water. *Adsorpt. Sci. Technol.* **2022**, *2022*, 4997205. [[CrossRef](#)]
21. Aruna; Bagotia, N.; Sharma, A.K.; Kumar, S. A review on modified sugarcane bagasse biosorbent for removal of dyes. *Chemosphere* **2021**, *268*, 129309. [[CrossRef](#)] [[PubMed](#)]
22. Amusat, S.O.; Kebede, T.G.; Dube, S.; Nindi, M.M. Ball-milling synthesis of biochar and biochar-based nanocomposites and prospects for removal of emerging contaminants: A review. *J. Water Process Eng.* **2021**, *41*, 101993. [[CrossRef](#)]
23. Kang, Z.; Jia, X.; Zhang, Y.; Kang, X.; Ge, M.; Liu, D.; Wang, C.; He, Z. A Review on Application of Biochar in the Removal of Pharmaceutical Pollutants through Adsorption and Persulfate-Based AOPs. *Sustainability* **2022**, *14*, 10128. [[CrossRef](#)]
24. Singh, M.; Ahsan, M.; Pandey, V.; Singh, A.; Mishra, D.; Tiwari, N.; Singh, P.; Karak, T.; Khare, P. Comparative assessment for removal of anionic dye from water by different waste-derived biochar vis a vis reusability of generated sludge. *Biochar* **2022**, *4*, 13. [[CrossRef](#)]
25. Gholami, P.; Khataee, A.; Soltani, R.; Dinpazhoh, L.; Bhatnagar, A. Photocatalytic degradation of gemifloxacin antibiotic using Zn-Co-LDH@biochar nanocomposite. *J. Hazard. Mater.* **2019**, *382*, 121070. [[CrossRef](#)]
26. El-Shafie, A.S.; Ahsan, I.; Radhwani, M.; Al-Khanghi, M.A.; El-Azazy, M. Synthesis and Application of Cobalt Oxide (Co₃O₄)-Impregnated Olive Stones Biochar for the Removal of Rifampicin and Tigecycline: Multivariate Controlled Performance. *Nanomaterials* **2022**, *12*, 379. [[CrossRef](#)]
27. Chakhtouna, H.; Benzeid, H.; Zari, N.; el kacem Qaiss, A.; Bouhfid, R. Functional CoFe₂O₄-modified biochar derived from banana pseudostem as an efficient adsorbent for the removal of amoxicillin from water. *Sep. Purif. Technol.* **2021**, *266*, 118592. [[CrossRef](#)]
28. Jiang, Z.; Wei, J.; Zhang, Y.; Niu, X.; Li, J.; Li, Y.; Pan, G.; Xu, M.; Cui, X.; Cui, N.; et al. Electron transfer mechanism mediated nitrogen-enriched biochar encapsulated cobalt nanoparticles catalyst as an effective persulfate activator for doxycycline removal. *J. Clean. Prod.* **2023**, *384*, 135641. [[CrossRef](#)]
29. Chen, L.; Li, F.; Wei, Y.; Li, G.; Shen, K.; He, H.-J. High cadmium adsorption on nanoscale zero-valent iron coated Eichhornia crassipes biochar. *Environ. Chem. Lett.* **2019**, *17*, 589–594. [[CrossRef](#)]
30. Zou, Y.; Wang, X.; Khan, A.; Wang, P.; Liu, Y.; Alsaedi, A.; Hayat, T.; Wang, X. Environmental Remediation and Application of Nanoscale Zero-Valent Iron and Its Composites for the Removal of Heavy Metal Ions: A Review. *Environ. Sci. Technol.* **2016**, *50*, 7290–7304. [[CrossRef](#)]
31. Yoadsomsuay, T.; Grisdanurak, N.; Liao, C.H. Influence of chitosan on modified nanoscale zero-valent iron for arsenate removal. *Desalination Water Treat.* **2016**, *57*, 17861–17869. [[CrossRef](#)]
32. Kumari, N.; Behera, M.; Singh, R. Facile synthesis of biopolymer decorated magnetic coreshells for enhanced removal of xenobiotic azo dyes through experimental modelling. *Food Chem. Toxicol. Int. J. Publ. Br. Ind. Biol. Res. Assoc.* **2023**, *171*, 113518. [[CrossRef](#)] [[PubMed](#)]

33. Mustafa, S.; Dilara, B.; Nargis, K.; Naeem, A.; Shahida, P. Surface properties of the mixed oxides of iron and silica. *Colloids Surf. A Physicochem. Eng. Aspects* **2002**, *205*, 273–282. [[CrossRef](#)]
34. Garg, U.K.; Kaur, M.P.; Garg, V.K.; Sud, D. Removal of nickel (II) from aqueous solution by adsorption on agricultural waste biomass using a response surface methodological approach. *Bioresour. Technol.* **2008**, *99*, 1325–1331. [[CrossRef](#)] [[PubMed](#)]
35. Cigeroğlu, Z.; Küçükyıldız, G.; Erim, B.; Alp, E. Easy preparation of magnetic nanoparticles-rGO-chitosan composite beads: Optimization study on cefixime removal based on RSM and ANN by using Genetic Algorithm Approach. *J. Mol. Struct.* **2021**, *1224*, 129182. [[CrossRef](#)]
36. Khoshnamvand, N.; Kord Mostafapour, F.; Mohammadi, A.; Faraji, M.J.A.E. Response surface methodology (RSM) modeling to improve removal of ciprofloxacin from aqueous solutions in photocatalytic process using copper oxide nanoparticles (CuO/UV). *AMB Express* **2018**, *8*, 48. [[CrossRef](#)]
37. Dash, A.R.; Lakhani, A.J.; Devi Priya, D.; Surendra, T.; Khan, M.M.R.; Samuel, E.; Roopan, S.M. Green Synthesis of Stannic Oxide Nanoparticles for Ciprofloxacin Degradation: Optimization and Modelling Using a Response Surface Methodology (RSM) Based on the Box–Behnken Design. *J. Clust. Sci.* **2023**, *34*, 121–133. [[CrossRef](#)]
38. Dey, S.; Al-Amin, M.; Rashid, T.; Sultan, Z.; Ashaduzzaman, M.; Sarker, M.; Shamsuddin, S. Preparation, characterization and performance evaluation of chitosan as an adsorbent for remazol red. *Int. J. Latest Res. Eng. Technol.* **2016**, *2*, 52–62.
39. Hao, G.; Hu, Y.; Shi, L.; Chen, J.; Cui, A.; Weng, W.; Osako, K. Physicochemical characteristics of chitosan from swimming crab (*Portunus trituberculatus*) shells prepared by subcritical water pretreatment. *Sci. Rep.* **2021**, *11*, 1646. [[CrossRef](#)]
40. Cui, L.; Wei, X.; Li, J.; Chang, G.; Huang, X.; Han, D. Structure and Saccharification of Sugarcane Bagasse Pretreated with Acid Coupled Alkaline. In *International Symposium on Mechanical Engineering and Material Science (ISMEMS 2017)*; Atlantis Press: Amsterdam, The Netherlands, 2017; pp. 104–107.
41. Shikuku, V.; Jemutai-Kimosop, S. Efficient Removal of Sulfamethoxazole onto Sugarcane Bagasse-derived Biochar: Two and Three-parameter Isotherms, Kinetics and Thermodynamics. *S. Afr. J. Chem. Suid Afrik. Tydskr. Vir Chem.* **2020**, *73*, 111–119.
42. Elshafai, M.; Hamdy, A.; Hefny, M. Zero-valent iron nanostructures: Synthesis, characterization and application. *J. Environ. Biotechnol* **2018**, *7*, 1–10.
43. Wang, Y.-Y.; You, L.-C.; Lyu, H.-H.; Liu, Y.-X.; He, L.-L.; Hu, Y.-D.; Luo, F.-C.; Yang, S.-M. Role of biochar–mineral composite amendment on the immobilization of heavy metals for Brassica chinensis from naturally contaminated soil. *Environ. Technol. Innov.* **2022**, *28*, 102622. [[CrossRef](#)]
44. Bagbi, Y.; Sarswat, A.; Tiwari, S.; Mohn, D.; Pandey, A.; R Solanki, P. Nanoscale zero-valent iron for aqueous lead removal. *Adv. Mater. Proc.* **2017**, *2*, 235–241.
45. Sun, L.; Chen, D.; Wan, S.; Yu, Z. Adsorption studies of dimetridazole and metronidazole onto biochar derived from sugarcane bagasse: Kinetic, equilibrium, and mechanisms. *J. Polym. Environ.* **2018**, *26*, 765–777. [[CrossRef](#)]
46. Rodier, L.; Bilba, K.; Onésippe, C.; Arsène, M.A. Utilization of bio-chars from sugarcane bagasse pyrolysis in cement-based composites. *Ind. Crops Prod.* **2019**, *141*, 111731. [[CrossRef](#)]
47. Drabczyk, A.; Kudłacik-Kramarczyk, S.; Głab, M.; Kędzierska, M.; Jaromin, A.; Mierzwiński, D.; Tylińczak, B. Physicochemical investigations of chitosan-based hydrogels containing Aloe Vera designed for biomedical use. *Materials* **2020**, *13*, 3073. [[CrossRef](#)]
48. Xu, H.; Gao, M.; Hu, X.; Chen, Y.; Li, Y.; Xu, X.; Zhang, R.; Yang, X.; Tang, C.; Hu, X. A novel preparation of S-nZVI and its high efficient removal of Cr(VI) in aqueous solution. *J. Hazard. Mater.* **2021**, *416*, 125924. [[CrossRef](#)]
49. Zheng, L.; Gao, Y.; Du, J.; Zhang, W.; Huang, Y.; Wang, L.; Zhao, Q.; Pan, X. A novel, recyclable magnetic biochar modified by chitosan–EDTA for the effective removal of Pb (II) from aqueous solution. *RSC Adv.* **2020**, *10*, 40196–40205. [[CrossRef](#)]
50. Zhang, M.; Liu, Y.; Li, T.; Xu, W.; Zheng, B.; Tan, X.; Wang, H.; Guo, Y.; Guo, F.; Wang, S. Chitosan modification of magnetic biochar produced from *Eichhornia crassipes* for enhanced sorption of Cr(VI) from aqueous solution. *RSC Adv.* **2015**, *5*, 46955–46964. [[CrossRef](#)]
51. Chen, X.L.; Li, F.; Xie, X.J.; Li, Z.; Chen, L. Nanoscale Zero-Valent Iron and Chitosan Functionalized *Eichhornia crassipes* Biochar for Efficient Hexavalent Chromium Removal. *Int. J. Environ. Res. Public Health* **2019**, *16*, 3046. [[CrossRef](#)]
52. Wang, J.; Zheng, S.; Shao, Y.; Liu, J.; Xu, Z.; Zhu, D. Amino-functionalized Fe₃O₄@SiO₂ core–shell magnetic nanomaterial as a novel adsorbent for aqueous heavy metals removal. *J. Colloid Interface Sci.* **2010**, *349*, 293–299. [[CrossRef](#)] [[PubMed](#)]
53. Castañeda Ramírez, A.A.; Rojas García, E.; López Medina, R.; Larios, J.L.C.; Suárez Parra, R.; Maubert Franco, A.M. Selective Adsorption of Aqueous Diclofenac Sodium, Naproxen Sodium, and Ibuprofen Using a Stable Fe(3)O(4)-FeBTC Metal-Organic Framework. *Materials* **2021**, *14*, 2293. [[CrossRef](#)] [[PubMed](#)]
54. Ahmaruzzaman, M. Biochar based nanocomposites for photocatalytic degradation of emerging organic pollutants from water and wastewater. *Mater. Res. Bull.* **2021**, *140*, 111262. [[CrossRef](#)]
55. Chausali, N.; Saxena, J.; Prasad, R. Nanobiochar and biochar based nanocomposites: Advances and applications. *J. Agric. Food Res.* **2021**, *5*, 100191. [[CrossRef](#)]
56. Chen, Z.; Wang, T.; Jin, X.; Chen, Z.; Megharaj, M.; Naidu, R. Multifunctional kaolinite-supported nanoscale zero-valent iron used for the adsorption and degradation of crystal violet in aqueous solution. *J. Colloid Interface Sci.* **2013**, *398*, 59–66. [[CrossRef](#)] [[PubMed](#)]
57. Wang, H.; Liu, R.; Chen, Q.; Mo, Y.; Zhang, Y. Biochar-supported starch/chitosan-stabilized nano-iron sulfide composites for the removal of lead ions and nitrogen from aqueous solutions. *Bioresour. Technol.* **2022**, *347*, 126700. [[CrossRef](#)]

58. Chen, G.; Wang, H.; Han, L.; Yang, N.; Hu, B.; Qiu, M.; Zhong, X. Highly efficient removal of U(VI) by a novel biochar supported with FeS nanoparticles and chitosan composites. *J. Mol. Liq.* **2021**, *327*, 114807. [[CrossRef](#)]
59. Yang, Y.; Zhang, Y.; Wang, G.; Yang, Z.; Xian, J.; Yang, Y.; Li, T.; Pu, Y.; Jia, Y.; Li, Y.; et al. Adsorption and reduction of Cr(VI) by a novel nanoscale FeS/chitosan/biochar composite from aqueous solution. *J. Environ. Chem. Eng.* **2021**, *9*, 105407. [[CrossRef](#)]
60. Shen, Q.; Wang, Z.; Yu, Q.; Cheng, Y.; Liu, Z.; Zhang, T.; Zhou, S. Removal of tetracycline from an aqueous solution using manganese dioxide modified biochar derived from Chinese herbal medicine residues. *Environ. Res.* **2020**, *183*, 109195. [[CrossRef](#)]
61. Behera, M.; Kumari, N.; Raza, K.; Singh, R. Fabrication of glutathione functionalized self-assembled magnetite nanochains for effective removal of crystal violet and phenol red dye from aqueous matrix. *Environ. Sci. Pollut. Res.* **2022**, *29*, 72260–72278. [[CrossRef](#)]
62. Mokete, R.; Eljamal, O.; Sugihara, Y. Exploration of the reactivity of nanoscale zero-valent iron (NZVI) associated nanoparticles in diverse experimental conditions. *Chem. Eng. Process. Process Intensif.* **2020**, *150*, 107879. [[CrossRef](#)]
63. Ouachtak, H.; El Guerdaoui, A.; El Haouti, R.; Haounati, R.; Ighnih, H.; Toubi, Y.; Alakhras, F.; Rehman, R.; Hafid, N.; Addi, A.A.; et al. Combined molecular dynamics simulations and experimental studies of the removal of cationic dyes on the eco-friendly adsorbent of activated carbon decorated montmorillonite Mt@AC. *RSC Adv.* **2023**, *13*, 5027–5044. [[CrossRef](#)]
64. Li, L.; Qiuling, M.; Wang, S.; Song, S.; Li, B.; Ruonan, G.; Cheng, X.; Cheng, Q. Photocatalytic Performance and Degradation Mechanism of Aspirin by TiO₂ through Response Surface Methodology. *Catalysts* **2018**, *8*, 118. [[CrossRef](#)]
65. Boushara, R.S.; Ngadi, N.; Wong, S.; Mohamud, M.Y. Removal of aspirin from aqueous solution using phosphoric acid modified coffee waste adsorbent. *Mater. Today Proc.* **2022**, *65*, 2960–2969. [[CrossRef](#)]
66. Mukoko, T.; Mupa, M.; Guyo, U.; Dziike, F. Preparation of Rice Hull Activated Carbon for the Removal of Selected Pharmaceutical Waste Compounds in Hospital Effluent. *J. Environ. Anal. Toxicol.* **2015**, *S7*, 008. [[CrossRef](#)]
67. Rocha, L.S.; Pereira, D.; Sousa, É.; Otero, M.; Esteves, V.I.; Calisto, V. Recent advances on the development and application of magnetic activated carbon and char for the removal of pharmaceutical compounds from waters: A review. *Sci. Total Environ.* **2020**, *718*, 137272. [[CrossRef](#)]
68. Shan, D.; Deng, S.; Zhao, T.; Wang, B.; Wang, Y.; Huang, J.; Yu, G.; Winglee, J.; Wiesner, M.R. Preparation of ultrafine magnetic biochar and activated carbon for pharmaceutical adsorption and subsequent degradation by ball milling. *J. Hazard. Mater.* **2016**, *305*, 156–163. [[CrossRef](#)]
69. Wong, K.T.; Yoon, Y.; Snyder, S.A.; Jang, M. Phenyl-functionalized magnetic palm-based powdered activated carbon for the effective removal of selected pharmaceutical and endocrine-disruptive compounds. *Chemosphere* **2016**, *152*, 71–80. [[CrossRef](#)]
70. Rajendran, K.; Sen, S. Adsorptive removal of carbamazepine using biosynthesized hematite nanoparticles. *Environ. Nanotechnol. Monit. Manag.* **2018**, *9*, 122–127. [[CrossRef](#)]
71. Nezhadali, A.; Koushali, S.E.; Divsar, F. Synthesis of polypyrrole-chitosan magnetic nanocomposite for the removal of carbamazepine from wastewater: Adsorption isotherm and kinetic study. *J. Environ. Chem. Eng.* **2021**, *9*, 105648. [[CrossRef](#)]
72. Shi, X.; Karachi, A.; Hosseini, M.; Yazd, M.S.; Kamyab, H.; Ebrahimi, M.; Parsaee, Z. Ultrasound wave assisted removal of Ceftriaxone sodium in aqueous media with novel nano composite g-C₃N₄/MWCNT/Bi₂WO₆ based on CCD-RSM model. *Ultrason. Sonochem.* **2020**, *68*, 104460. [[CrossRef](#)] [[PubMed](#)]
73. Yousefi, M.; Gholami, M.; Oskoei, V.; Mohammadi, A.A.; Baziar, M.; Esrafil, A. Comparison of LSSVM and RSM in simulating the removal of ciprofloxacin from aqueous solutions using magnetization of functionalized multi-walled carbon nanotubes: Process optimization using GA and RSM techniques. *J. Environ. Chem. Eng.* **2021**, *9*, 105677. [[CrossRef](#)]
74. Dargahi, A.; Samarghandi, M.R.; Shabanloo, A.; Mahmoudi, M.M.; Nasab, H.Z. Statistical modeling of phenolic compounds adsorption onto low-cost adsorbent prepared from aloe vera leaves wastes using CCD-RSM optimization: Effect of parameters, isotherm, and kinetic studies. *Biomass Convers. Biorefin.* **2021**, *5*, 1–15. [[CrossRef](#)]
75. Saputra, E.; Muhammad, S.; Sun, H.; Ang, H.M.; Tadó, M.O.; Wang, S. Different Crystallographic One-dimensional MnO₂ Nanomaterials and Their Superior Performance in Catalytic Phenol Degradation. *Environ. Sci. Technol.* **2013**, *47*, 5882–5887. [[CrossRef](#)]
76. Zhang, L.; Zhao, X.; Niu, C.; Tang, N.; Guo, H.; Wen, X.; Liang, C.; Zeng, G. Enhanced activation of peroxydisulfate by magnetic Co₃MnFeO₆ nanoparticles for removal of carbamazepine: Efficiency, synergetic mechanism and stability. *Chem. Eng. J.* **2019**, *362*, 851–864. [[CrossRef](#)]
77. Langeroudi, M.P.; Binaeian, E. Tannin-APTES modified Fe₃O₄ nanoparticles as a carrier of Methotrexate drug: Kinetic, isotherm and thermodynamic studies. *Mater. Chem. Phys.* **2018**, *218*, 210–217. [[CrossRef](#)]
78. Binaeian, E.; Seghatoleslami, N.; Chaichi, M.J. Synthesis of oak gall tannin-immobilized hexagonal mesoporous silicate (OGT-HMS) as a new super adsorbent for the removal of anionic dye from aqueous solution. *Desalination Water Treat.* **2016**, *57*, 8420–8436. [[CrossRef](#)]
79. Akpomie, K.G.; Conradie, J. Isotherm, kinetic, thermodynamics and reusability data on the adsorption of antidepressant onto silver nanoparticle-loaded biowaste. *Data Brief* **2021**, *39*, 107575. [[CrossRef](#)]
80. Ho, Y.-S. Review of second-order models for adsorption systems. *J. Hazard. Mater.* **2006**, *136*, 681–689. [[CrossRef](#)]
81. Bhattacharya, S.; Banerjee, D.P.; Das, P.; Bhowal, A.; Majumdar, S.; Ghosh, P. Removal of aqueous carbamazepine using graphene oxide nanoplatelets: Process modelling and optimization. *Sustain. Environ. Res.* **2020**, *30*, 17. [[CrossRef](#)]
82. Weber, W.J., Jr.; Morris, J.C. Kinetics of adsorption on carbon from solution. *J. Sanit. Eng. Div.* **1963**, *89*, 31–59. [[CrossRef](#)]

83. Moreno-Marengo, A.R.; Giraldo, L.; Moreno-Piraján, J.C. Parabens Adsorption onto Activated Carbon: Relation with Chemical and Structural Properties. *Molecules* **2019**, *24*, 4313. [[CrossRef](#)]
84. Moawed, E.A.; El-Shahat, M.F. Equilibrium, kinetic and thermodynamic studies of the removal of triphenyl methane dyes from wastewater using iodopolyurethane powder. *J. Taibah Univ. Sci.* **2016**, *10*, 46–55. [[CrossRef](#)]
85. Zhang, L.; Zeng, Y.; Cheng, Z. Removal of heavy metal ions using chitosan and modified chitosan: A review. *J. Mol. Liq.* **2016**, *214*, 175–191. [[CrossRef](#)]
86. Hadizade, G.; Binaeian, E.; Emami, M.R.S. Preparation and characterization of hexagonal mesoporous silica/polyacrylamide nanocomposite capsule (PAM-HMS) for dye removal from aqueous solutions. *J. Mol. Liq.* **2017**, *238*, 499–507. [[CrossRef](#)]
87. Ayawei, N.; Ebelegi, A.N.; Wankasi, D. Modelling and Interpretation of Adsorption Isotherms. *J. Chem.* **2017**, *2017*, 3039817. [[CrossRef](#)]
88. Teixeira, S.; Gurke, R.; Eckert, H.; Kühn, K.; Fauler, J.; Cuniberti, G. Photocatalytic degradation of pharmaceuticals present in conventional treated wastewater by nanoparticle suspensions. *J. Environ. Chem. Eng.* **2016**, *4*, 287–292. [[CrossRef](#)]
89. Décima, M.A.; Marzeddu, S.; Barchiesi, M.; Di Marcantonio, C.; Chiavola, A.; Boni, M.R. A Review on the Removal of Carbamazepine from Aqueous Solution by Using Activated Carbon and Biochar. *Sustainability* **2021**, *13*, 11760. [[CrossRef](#)]
90. Naghdi, M.; Taheran, M.; Pulicharla, R.; Rouissi, T.; Brar, S.K.; Verma, M.; Surampalli, R.Y. Pine-wood derived nanobiochar for removal of carbamazepine from aqueous media: Adsorption behavior and influential parameters. *Arab. J. Chem.* **2019**, *12*, 5292–5301. [[CrossRef](#)]
91. Chegeni, M.; Mousavi, Z.; Soleymani, M.; Dehdashtian, S. Removal of aspirin from aqueous solutions using graphitic carbon nitride nanosheet: Theoretical and experimental studies. *Diam. Relat. Mater.* **2020**, *101*, 107621. [[CrossRef](#)]
92. Abdel-Aziz, H.M.; Farag, R.S.; Abdel-Gawad, S.A. Carbamazepine Removal from Aqueous Solution by Green Synthesis Zero-Valent Iron/Cu Nanoparticles with Ficus Benjamina Leaves' Extract. *Int. J. Environ. Res.* **2019**, *13*, 843–852. [[CrossRef](#)]
93. Wei, H.; Deng, S.; Huang, Q.; Nie, Y.; Wang, B.; Huang, J.; Yu, G. Regenerable granular carbon nanotubes/alumina hybrid adsorbents for diclofenac sodium and carbamazepine removal from aqueous solution. *Water Res.* **2013**, *47*, 4139–4147. [[CrossRef](#)] [[PubMed](#)]
94. Ji, L.; Chen, W.; Duan, L.; Zhu, D. Mechanisms for strong adsorption of tetracycline to carbon nanotubes: A comparative study using activated carbon and graphite as adsorbents. *Environ. Sci. Technol.* **2009**, *43*, 2322–2327. [[CrossRef](#)] [[PubMed](#)]
95. Al-Khateeb, L.A.; Almotiry, S.; Salam, M.A. Adsorption of pharmaceutical pollutants onto graphene nanoplatelets. *Chem. Eng. J.* **2014**, *248*, 191–199. [[CrossRef](#)]

Disclaimer/Publisher's Note: The statements, opinions and data contained in all publications are solely those of the individual author(s) and contributor(s) and not of MDPI and/or the editor(s). MDPI and/or the editor(s) disclaim responsibility for any injury to people or property resulting from any ideas, methods, instructions or products referred to in the content.